3^{++} light meson family

Hao Chen,[1] Yan-Yue Fan,[1] Yun-Hai Zhang,[2] and Cheng-Qun Pang[3,4,*]

[1]*College of Physics and Electronic Information Engineering, Qinghai Normal University, Xining 810000, China*

[2]*College of Physics and Electronic Engineering, Heze University, Heze 274015, China*

[3]*School of Physics and Optoelectronic Engineering, Ludong University, Yantai 264000, China*

[4]*Lanzhou Center for Theoretical Physics, Key Laboratory of Quantum Theory and Applications of MoE, and Key Laboratory of Theoretical Physics of Gansu Province, Lanzhou University, Lanzhou, Gansu 730000, China*

(Received 21 October 2025; revised 13 February 2026; accepted 16 March 2026; published 6 April 2026)

The spectroscopy of the 3^{++} light-meson candidates, in particular the a_3 and f_3 families, remains an open issue. We compute the mass spectra in the modified Godfrey-Isgur model and evaluate the Okubo-Zweig-Iizuka-allowed two-body strong decays within the quark-pair-creation model. Our analysis favors the interpretation that $a_3(1875)$ and $a_3(2030)$ correspond to the same resonance, identified as the a_3 ground state, while $f_3(2050)$ is the ground state of the f_3 family; furthermore, $a_3(2275)$ and $f_3(2300)$ are assigned as their first radial excited states. For other higher-excitation states, we provide predictions for the decay behaviors and include the mass-induced model uncertainty.

DOI: 10.1103/zmyc-9h8f

I. INTRODUCTION

The spectroscopy of light mesons plays a crucial role in exploring the nonperturbative regime of QCD. Among the various meson families, higher-spin states provide essential tests for quark-model predictions. In this context, investigations of the a_3, f_3, and f_3' meson families are of particular interest.

The a_3 and f_3 meson families are characterized by $J^{PC} = 3^{++}$ (with P and C denoting spatial parity and charge conjugation parity, respectively), which corresponds to spin $S = 1$, orbital angular momentum $L = 3$, and total angular momentum $J = 3$. In particular, the isovector states with $I^G = 1^-$, referred to as the a_3 family, and the isoscalar states with $I^G = 0^+$, referred to as the f_3 and f_3' families, have attracted sustained attention. Several members, such as $a_3(1875)$, $a_3(2030)$, $a_3(2275)$, $f_3(2050)$, and $f_3(2300)$, are listed in the Particle Data Group (PDG), with their masses, widths, and branching ratios reported by a variety of experiments [1].

Experimental studies of the 3^{++} light-meson family date back to the early 2000s. The $a_3(1875)$ resonance was reported by the E852 Collaboration in a partial-wave analysis (PWA) of the reaction $\pi^- p \to \pi^+\pi^-\pi^- p$ at 18 GeV/c [2]. Subsequently, the Crystal Barrel Collaboration at LEAR reported two higher isovector states in $\bar{p}p$ annihilation: $a_3(2030)$ and $a_3(2275)$ [3,4].

For the isoscalar sector, a pronounced 3^{++} signal identified as $f_3(2050)$ was observed in $\bar{p}p$ annihilation into several final states, notably $\bar{p}p \to \eta\pi^0\pi^0$, $\pi^0\pi^0$, $\pi^+\pi^-$, $\eta\eta$, and $\eta\eta'$ [5]. A heavier isoscalar partner, $f_3(2300)$, was subsequently reported via a dedicated PWA of $\bar{p}p \to \Lambda\bar{\Lambda}$ data [6].

Regarding spectroscopic assignments, Refs. [7,8] suggest that $a_3(1875)$ and $a_3(2030)$ may be the same state, serving as the ground state of the a_3 family, with $a_3(2275)$ as its first radial excitation. By contrast, the relativistic quark-model spectra by Ebert *et al.* assign $a_3(1875)$ as the a_3 ground state and identify $a_3(2030)$ and $a_3(2275)$ as the first and second radial excitations, respectively [9].

References [5,8,10] interpret $f_3(2050)$ as the 1^3F_3 ground state and $f_3(2300)$ as its first radial excitation, whereas Ref. [7] proposes that $f_3(2050)$ and $f_3(2300)$ correspond to the first and second radial excitations, respectively, thereby implying an unobserved ground f_3 state near 1.7 GeV. A quasipotential relativistic quark-model calculation by Ebert *et al.* further suggests that $f_3(2300)$ could be the ground state of the f_3 family with a dominant strangeonium component [9].

*Contact author: xuehua45@163.com

Published by the American Physical Society under the terms of the Creative Commons Attribution 4.0 International license. Further distribution of this work must maintain attribution to the author(s) and the published article's title, journal citation, and DOI. Funded by SCOAP³.

For the isoscalar members of the 3^{++} family, f_3 and f_3' are mixtures of the nonstrange and strange flavor-basis states, given by

$$\begin{pmatrix} f_3(nF) \\ f_3'(nF) \end{pmatrix} = \begin{pmatrix} \cos\theta_{n^3F_3} & \sin\theta_{n^3F_3} \\ -\sin\theta_{n^3F_3} & \cos\theta_{n^3F_3} \end{pmatrix} \begin{pmatrix} |n\bar{n}\rangle \\ |s\bar{s}\rangle \end{pmatrix}, \quad (1.1)$$

where $n\bar{n} = \frac{u\bar{u}+(-1)^I d\bar{d}}{\sqrt{2}}$, with u, d, and s denoting the up, down, and strange quarks, respectively.

Reference [11] reports a nonstrange–strange mixing angle for the $f_3(1F)$ meson of $\theta_{1^3F_3} = 3 \pm 2°$. Testing this mixing angle for $f_3(1F)$ meson and studying the mixing angle of other f_3 mesons through their decay properties can help us better understand their internal structures.

As previously mentioned, the classification of the 3^{++} light mesons remains controversial, making the establishment of their spectroscopic assignments an interesting and important research issue.

In potential models describing the light meson spectrum, the one-gluon exchange (OGE) and linear confinement are generally included as the core components. In 1985, Godfrey and Isgur developed a relativized quark model [known as the Godfrey-Isgur (GI) model] incorporating these contributions. Over the past 40 years, the GI model has been widely used to investigate meson spectra [12,13]. More recently, the modified GI (MGI) model, which incorporates color screening effects [14–18], has been successfully applied to doubly heavy-flavor mesons, light mesons, and baryons [19–22]. For describing the nature of the higher-spin 3^{++} light-meson family, the MGI model is adopted to study their spectroscopic properties.

In our previous work, we have adopted the MGI model to predict the spectroscopic properties of the 5^{++} and 4^{++} meson families [23,24]. In those studies, we also employed the quark-pair creation (QPC) model, also known as the $^3P_0$ model [25,26], to predict their two-body strong decays. In this work, we employ these two models to study the spectra and two-body strong decays of the 3^{++} family. We aim to clarify the spectroscopic assignments of $a_3(1875)$, $a_3(2030)$, $a_3(2275)$, $f_3(2050)$, and $f_3(2300)$, and to provide decay-behavior predictions that may guide future experimental measurements and help establish the 3^{++} meson family.

The paper is organized as follows. In Sec. II, we briefly review the MGI model and the $^3P_0$ model. Section III presents our numerical results for the 3^{++} family; first, we verify the assignments of the $a_3(1875)$, $a_3(2030)$, $a_3(2275)$, $f_3(2050)$, and $f_3(2300)$, and then provide predictions for higher 3^{++} states. Conclusions are given in Sec. IV.

II. MODELS EMPLOYED IN THIS WORK

In the following part, spectroscopy (masses and wave functions) is computed using a screened and relativistic quark potential (the MGI model), and the Okubo-Zweig-Iizuka (OZI)-allowed two-body strong decay widths are evaluated in the QPC model. Both models are introduced below.

A. The modified GI model

Building on the GI model, which achieved notable success in describing relativistic meson spectrum—especially the low-lying states [12], Song *et al.* developed the MGI model [19]. By incorporating a screened confining potential that is softened at large distances to mimic string breaking, as suggested by unquenched lattice QCD [14–16,27], the MGI model provides an improved description of excited charmed and charmed-strange mesons in Ref. [19]. Since its introduction, it has been applied to light-meson spectroscopy [28–33], double-heavy quarkonia [20,21], and baryons [22]. The Hamiltonian of the MGI model reads,

$$\tilde{H} = \sum_i \sqrt{m_i^2 + \mathbf{p}^2} + \tilde{V}^{\text{eff}}, \quad (2.1)$$

where m_i denotes the mass of the constituent quark (or antiquark) and $\mathbf{p}$ is the three-momentum of either constituent. Throughout, we take $m_{u(d)} = 0.162$ GeV for the $u(d)$ and $m_s = 0.377$ GeV for the s (see Table I). The effective potential is decomposed as

$$\tilde{V}^{\text{eff}} = \tilde{G}_{12} + \tilde{V}^{\text{cont}} + \tilde{V}^{\text{tens}} + \tilde{V}^{\text{so(v)}} + \tilde{S}_{12}(r) + \tilde{V}^{\text{so(s)}}, \quad (2.2)$$

with the following interpretation for each term:

TABLE I. Parameters of the MGI model [33]. $m_{u(d)}$ and m_s are the masses of the $u(d)$ and s quarks (or antiquarks), μ is the screening parameter, b is the confining parameter, and c is the vacuum constant. σ_0 is the universal parameter in Eq. (2.6), while s is a parameter related to heavy quarkonium masses. ϵ_c, ϵ_t, $\epsilon_{\text{so(v)}}$, and $\epsilon_{\text{so(s)}}$ represent the relativistic corrections to the potential terms $\tilde{V}^{\text{cont}}$, $\tilde{V}^{\text{tens}}$, $\tilde{V}^{\text{so(v)}}$, and $\tilde{V}^{\text{so(s)}}$, respectively. $\gamma = 5.1$ is fitted with the total width of $a_3(2030)(1F)$, $a_3(2275)(2F)$, $f_3(2050)(1F)(\theta_{1^3F_3} = 0)$, and $f_3(2300)(2F)(\theta_{2^3F_3} = 0)$.

Parameter	Value	Parameter	Value
$m_{u(d)}$ (GeV)	0.162	s	0.711
m_s (GeV)	0.377	μ (GeV)	0.0779
b (GeV^2)	0.222	c (GeV)	−0.228
ϵ_c	−0.137	$\epsilon_{so(v)}$	0.0550
$\epsilon_{so(s)}$	0.366	ϵ_t	0.493
σ_0 (GeV)	1.791	γ	5.1

(i) $\tilde{G}_{12}$: the (smeared) one-gluon-exchange (OGE) potential;
(ii) $\tilde{V}^{\rm cont}$: the short-range spin-spin contact potential;
(iii) $\tilde{V}^{\rm tens}$: the tensor interaction from OGE;
(iv) $\tilde{V}^{\rm so(v)}$: the vector spin-orbit contribution;
(v) $\tilde{S}_{12}(r)$: the screened confining potential that encodes color screening;
(vi) $\tilde{V}^{\rm so(s)}$: the scalar spin-orbit contribution.

Explicit expressions and detailed discussions of these potential terms are presented below.

In the nonrelativistic limit, one of the spin-independent central term takes the form

$$\tilde{G}(r) = -\sum_{k=1}^{3}\frac{4\alpha_k}{3r}\left[\frac{2}{\sqrt{\pi}}\int_0^{\gamma_k r} e^{-x^2}\,\mathrm{d}x\right], \tag{2.3}$$

with the effective strong-coupling coefficients $(\alpha_1,\alpha_2,\alpha_3) = (0.25, 0.15, 0.20)$ and the range parameters $(\gamma_1,\gamma_2,\gamma_3) = (1/2\ \text{GeV}, \sqrt{10}/2\ \text{GeV}, \sqrt{1000}/2\ \text{GeV})$ [12], while the other is given by

$$S(r) = \frac{b(1-e^{-\mu r})}{\mu} + c, \tag{2.4}$$

where we adopt the screening parameter $\mu = 0.0779$ GeV from our previous work [33]. This parameter controls the strength of color screening; it is absent in the original GI model and thus constitutes a key refinement in the MGI framework. We set $b = 0.222\ \text{GeV}^2$ for the string tension and $c = -0.228$ GeV for the constant term [33].

The relativistic effects are incorporated in two ways. First, the internal motion of the constituents and the nonlocality of the $q\bar{q}$ interaction are modeled through a mass-dependent Gaussian smearing function $\rho_{ij}(\mathbf{r}-\mathbf{r}')$,

$$\rho_{ij}(\mathbf{r}-\mathbf{r}') = \frac{\sigma_{ij}^3}{\pi^{3/2}}\exp[-\sigma_{ij}^2(\mathbf{r}-\mathbf{r}')^2], \tag{2.5}$$

with

$$\sigma_{ij}^2 = \sigma_0^2\left[\frac{1}{2}+\frac{1}{2}\left(\frac{4m_i m_j}{(m_i+m_j)^2}\right)^4\right] + s^2\left(\frac{2m_i m_j}{m_i+m_j}\right)^2, \tag{2.6}$$

where $\sigma_0 = 1.791$ GeV and $s = 0.711$ are the universal parameters, with values taken from Ref. [33]. This smearing is applied to the central OGE Coulomb kernel $G(r)$ and the screened confinement $S(r)$ as follows:

$$\begin{aligned}\tilde{G}_{ij}(r) &= \int \mathrm{d}^3\mathbf{r}'\rho_{ij}(\mathbf{r}-\mathbf{r}')G(r') \\ &= -\sum_{k=1}^{3}\frac{4\alpha_k}{3r}\mathrm{erf}(\tau_{kij}r),\end{aligned} \tag{2.7}$$

where

$$\tau_{kij} = \frac{1}{\sqrt{\frac{1}{\sigma_{ij}^2}+\frac{1}{\gamma_k^2}}}, \tag{2.8}$$

and

$$\begin{aligned}\tilde{S}_{12}(r) &= \int \mathrm{d}^3\mathbf{r}'\rho_{12}(\mathbf{r}-\mathbf{r}')S(r') \\ &= \frac{b}{\mu r}\left[r + e^{\frac{\mu^2}{4\sigma^2}+\mu r}\frac{\mu+2r\sigma^2}{2\sigma^2}\left(\frac{1}{\sqrt{\pi}}\int_0^{\frac{\mu+2r\sigma^2}{2\sigma}} e^{-x^2}\mathrm{d}x - \frac{1}{2}\right)\right. \\ &\quad \left. - e^{\frac{\mu^2}{4\sigma^2}-\mu r}\frac{\mu-2r\sigma^2}{2\sigma^2}\left(\frac{1}{\sqrt{\pi}}\int_0^{\frac{\mu-2r\sigma^2}{2\sigma}} e^{-x^2}\mathrm{d}x - \frac{1}{2}\right)\right] + c,\end{aligned}$$

with $\sigma \equiv \sigma_{12}$. The spin-dependent interactions (contact, tensor, spin-orbit) are then constructed from these smeared central kernels (see below).

Second, relativistic kinematics is incorporated through momentum-dependent similarity factors that reduce to unity in the nonrelativistic limit. Accordingly, the smeared Coulomb term is modified as

$$\tilde{G}_{12}(r) \longrightarrow \left(1+\frac{\mathbf{p}^2}{E_1E_2}\right)^{1/2}\tilde{G}_{12}(r)\left(1+\frac{\mathbf{p}^2}{E_1E_2}\right)^{1/2}, \tag{2.9}$$

where $E_{1(2)} = \sqrt{m_{1(2)}^2+\mathbf{p}^2}$. Similarly, the spin-dependent operators built from the smeared kernels are modified by semirelativistic corrections via

$$\tilde{V}^i_{\alpha\beta} = \left(\frac{m_\alpha m_\beta}{E_\alpha E_\beta}\right)^{1/2+\epsilon_i}\tilde{V}^i_{\alpha\beta}(r)\left(\frac{m_\alpha m_\beta}{E_\alpha E_\beta}\right)^{1/2+\epsilon_i}, \tag{2.10}$$

where i labels the four spin-dependent components; $i = \{\text{cont}, \text{tens}, \text{so(v)}, \text{so(s)}\}$, and the corresponding exponents $\epsilon_i = \{\epsilon_c, \epsilon_t, \epsilon_{\text{so(v)}}, \epsilon_{\text{so(s)}}\}$ represent the relativistic corrections to $\tilde{V}^{\rm cont}$, $\tilde{V}^{\rm tens}$, $\tilde{V}^{\rm so(v)}$, and $\tilde{V}^{\rm so(s)}$, respectively. Their values are taken from Ref. [30] and listed in Table I.

Then the explicit spin-dependent potentials, expressed in terms of the smeared OGE and confinement kernels, read

$$\tilde{V}^{\rm cont} = \frac{2\mathbf{S}_1\cdot\mathbf{S}_2}{3m_1m_2}\nabla^2\tilde{G}^c_{12}, \tag{2.11}$$

$$\tilde{V}^{\rm tens} = -\frac{3(\mathbf{S}_1\cdot\hat{\mathbf{r}})(\mathbf{S}_2\cdot\hat{\mathbf{r}})-\mathbf{S}_1\cdot\mathbf{S}_2}{3m_1m_2}\left(\frac{\mathrm{d}^2}{\mathrm{d}r^2}-\frac{1}{r}\frac{\mathrm{d}}{\mathrm{d}r}\right)\tilde{G}^t_{12}, \tag{2.12}$$

$$\begin{aligned}\tilde{V}^{\rm so(v)} &= \frac{\mathbf{S}_1\cdot\mathbf{L}}{2m_1^2}\frac{1}{r}\frac{\mathrm{d}\tilde{G}^{\rm so(v)}_{11}}{\mathrm{d}r} + \frac{\mathbf{S}_2\cdot\mathbf{L}}{2m_2^2}\frac{1}{r}\frac{\mathrm{d}\tilde{G}^{\rm so(v)}_{22}}{\mathrm{d}r} \\ &\quad + \frac{(\mathbf{S}_1+\mathbf{S}_2)\cdot\mathbf{L}}{m_1m_2}\frac{1}{r}\frac{\mathrm{d}\tilde{G}^{\rm so(v)}_{12}}{\mathrm{d}r},\end{aligned} \tag{2.13}$$

$$\tilde{V}^{\mathrm{so(s)}} = -\frac{\mathbf{S}_1\cdot\mathbf{L}}{2m_1^2}\frac{1}{r}\frac{\mathrm{d}\tilde{S}_{11}^{\mathrm{so(s)}}}{\mathrm{d}r} - \frac{\mathbf{S}_2\cdot\mathbf{L}}{2m_2^2}\frac{1}{r}\frac{\mathrm{d}\tilde{S}_{22}^{\mathrm{so(s)}}}{\mathrm{d}r}. \tag{2.14}$$

We obtain the light meson spectrum by expanding the states in a simple-harmonic-oscillator (SHO) basis. The SHO eigenfunctions are

$$\begin{aligned}\psi^{\mathrm{SHO}}_{nLM_L}(\mathbf{r}) &= R^{\mathrm{SHO}}_{nL}(r,\beta)Y_{LM_L}(\Omega_r),\\ \psi^{\mathrm{SHO}}_{nLM_L}(\mathbf{p}) &= R^{\mathrm{SHO}}_{nL}(p,\beta)Y_{LM_L}(\Omega_p),\end{aligned} \tag{2.15}$$

with radial parts,

$$R^{\mathrm{SHO}}_{nL}(r,\beta) = N_{nL}\beta^{3/2}(\beta r)^L e^{-\beta^2 r^2/2}L_{n-1}^{L+1/2}(\beta^2 r^2), \tag{2.16}$$

$$\begin{aligned}R^{\mathrm{SHO}}_{nL}(p,\beta) = \frac{(-1)^{n-1}(-i)^L}{\beta^{3/2}}N_{nL}e^{-p^2/(2\beta^2)}\left(\frac{p}{\beta}\right)^L\\ \times L_{n-1}^{L+1/2}\left(\frac{p^2}{\beta^2}\right),\end{aligned} \tag{2.17}$$

and the normalization constant,

$$N_{nL} = \sqrt{\frac{2(n-1)!}{\Gamma(n+L+1/2)}}. \tag{2.18}$$

Here, $Y_{LM_L}(\Omega)$ are the spherical harmonics, $L_{n-1}^{L+1/2}(x)$ represent the associated Laguerre polynomials, and $\Gamma(\cdot)$ denotes the gamma function.

In this representation, the radial wave functions of the light $q\bar{q}$ mesons under study are expanded as

$$R_{nL}(r) = \sum_{k=1}^{N_{\max}} C_k R^{\mathrm{SHO}}_{kL}(r,\beta), \tag{2.19}$$

$$R_{nL}(p) = \sum_{k=1}^{N_{\max}} C_k R^{\mathrm{SHO}}_{kL}(p,\beta), \tag{2.20}$$

where the coefficients C_k are obtained by diagonalizing the Hamiltonian in Eq. (2.1), and we employ $N_{\max} = 21$ basis functions in our numerical calculations. The SHO basis depends on a single scale parameter β; for each meson i we fix β_i variationally by minimizing the eigenvalue E_{nL}, i.e., $\partial E_{nL}/\partial\beta_i = 0$ and $\partial^2 E_{nL}/\partial\beta_i^2 > 0$. Some of the corresponding β values can be found in Ref. [34]. The resulting spatial wave functions from the MGI model are then used as inputs for the strong-decay calculations.

B. The QPC model

The QPC model was first proposed by Micu [25] and later developed by the Orsay group [35–39]. It has since been widely applied to the study of OZI-allowed two-body strong decays of mesons [26,28–32,40–61]. Within this framework, the transition operator $\mathcal{T}$ creates a quark-antiquark pair (labeled 3 and 4) from the vacuum with quantum numbers $^{2S+1}L_J = {}^3P_0$. For the process $A\to B+C$, $\mathcal{T}$ can be expressed as

$$\begin{aligned}\mathcal{T} = -3\gamma\sum_m\langle 1m;1-m|00\rangle\int \mathrm{d}^3\mathbf{p}_3\mathrm{d}^3\mathbf{p}_4\delta^3(\mathbf{p}_3+\mathbf{p}_4)\\ \times\mathcal{Y}_{1m}\left(\frac{\mathbf{p}_3-\mathbf{p}_4}{2}\right)\chi^{34}_{1,-m}\phi^{34}_0(\omega^{34}_0)_{ij}b^\dagger_{3i}(\mathbf{p}_3)d^\dagger_{4j}(\mathbf{p}_4).\end{aligned} \tag{2.21}$$

Here, the parameter γ in the QPC model characterizes the strength of $q\bar{q}$-pair creation from the vacuum. In the present work, the value $\gamma = 5.1$ is determined by fitting to the total widths of $a_3(2030)(1F)$, $a_3(2275)(2F)$, $f_3(2050)(1F)$ $(\theta_{1^3F_3}=0)$, and $f_3(2300)(2F)$ $(\theta_{2^3F_3}=0)$ with their experimental masses taken as inputs. The function $\mathcal{Y}^m_l(\mathbf{p}) \equiv p^l Y^m_l(\theta_p,\phi_p)$ denotes a solid harmonic, while χ, ϕ, and ω represent the spin, flavor, and color wave functions, respectively. $\mathbf{p_3}$ and $\mathbf{p_4}$ are the three-momenta of the quark and antiquark created from the vacuum, while i and j denote their color indices. With this transition operator, the decay amplitudes of mesons can be systematically evaluated within the QPC framework. The amplitude $\mathcal{M}^{M_{J_\mathrm{A}}M_{J_\mathrm{B}}M_{J_\mathrm{C}}}$ is defined as

$$\langle \mathrm{BC}|\mathcal{T}|\mathrm{A}\rangle = \delta^3(\mathbf{P}_\mathrm{B}+\mathbf{P}_\mathrm{C})\mathcal{M}^{M_{J_\mathrm{A}}M_{J_\mathrm{B}}M_{J_\mathrm{C}}}, \tag{2.22}$$

where $\mathbf{P}_\mathrm{B}$ and $\mathbf{P}_\mathrm{C}$ are the three-momenta of mesons B and C in the rest frame of the initial meson A, and M_{J_i} $(i=\mathrm{A},\mathrm{B},\mathrm{C})$ denotes the corresponding magnetic quantum numbers. The partial width takes the form,

$$\Gamma_{\mathrm{A}\to\mathrm{BC}} = \frac{\pi}{4}\frac{|\mathbf{P}|}{m_\mathrm{A}^2}\sum_{J,L}|\mathcal{M}^{JL}(\mathbf{P})|^2, \tag{2.23}$$

where m_A is the mass of meson A, $\mathbf{P}\equiv\mathbf{P}_\mathrm{B}$, L is the relative orbital angular momentum between B and C, and J represents the total angular momentum resultant from coupling $\mathbf{J}=\mathbf{J}_\mathrm{B}+\mathbf{J}_\mathrm{C}$. The partial-wave amplitude $\mathcal{M}^{JL}(\mathbf{P})$ is related to the amplitude $\mathcal{M}^{M_{J_\mathrm{A}}M_{J_\mathrm{B}}M_{J_\mathrm{C}}}$ via the Jacob-Wick transformation [62],

$$\begin{aligned}\mathcal{M}^{JL}(\mathbf{P}) = \frac{\sqrt{4\pi(2L+1)}}{2J_\mathrm{A}+1}\sum_{M_{J_\mathrm{B}}M_{J_\mathrm{C}}}\langle L0;JM_{J_\mathrm{A}}|J_\mathrm{A}M_{J_\mathrm{A}}\rangle\\ \times\langle J_\mathrm{B}M_{J_\mathrm{B}};J_\mathrm{C}M_{J_\mathrm{C}}|J_\mathrm{A}M_{J_\mathrm{A}}\rangle\mathcal{M}^{M_{J_\mathrm{A}}M_{J_\mathrm{B}}M_{J_\mathrm{C}}},\end{aligned} \tag{2.24}$$

in which

$$\mathcal{M}^{M_{J_A}M_{J_B}M_{J_C}} = \gamma \sum_{\substack{M_{L_A},M_{S_A},M_{L_B},\\ M_{S_B}M_{L_C},M_S,m}} \langle L_A M_{L_A} S_A M_{S_A}|J_A M_{J_A}\rangle \times \langle L_B M_{L_B} S_B M_{S_B}|J_B M_{J_B}\rangle \langle L_C M_{L_C} S_C M_{S_C}|J_C M_{J_C}\rangle \langle 1m1-m|00\rangle \langle \chi^{14}_{S_B M_{S_B}} \chi^{32}_{S_C M_{S_C}}|\chi^{12}_{S_A M_{S_A}} \chi^{34}_{1-m}\rangle \times [\langle \phi^{14}_B \phi^{32}_C|\phi^{12}_A \phi^{34}_0\rangle I(\mathbf{P}, m_1, m_2, m_3) + (-1)^{1+S_A+S_B+S_C+L_C} \langle \phi^{32}_B \phi^{14}_C|\phi^{12}_A \phi^{34}_0\rangle I(-\mathbf{P}, m_2, m_1, m_3)], \quad (2.25)$$

with the overlap integral

$$I(\mathbf{P}, m_1, m_2, m_3) = \int \mathrm{d}^3\mathbf{k} \psi^*_B(\mathbf{k} + U\mathbf{P}) \psi^*_C(\mathbf{k} + V\mathbf{P}) \psi_A(\mathbf{k} - \mathbf{P}) \mathcal{Y}^m_1(\mathbf{k}), \quad (2.26)$$

where

$$U = \frac{m_3}{m_1 + m_3}, \qquad V = \frac{m_3}{m_2 + m_3}.$$

Here, m_1 and m_2 are the constituent quark and antiquark masses in the initial meson A. In our calculations, we take $(m_1, m_2) = (0.377, 0.162)$ GeV for $s\bar{n}$, (0.162, 0.162) GeV for $n\bar{n}$, and (0.377, 0.377) GeV for $s\bar{s}$. The mass of the created quark (or antiquark) is $m_3 = 0.162$ GeV for $n\bar{n}$ creation and $m_3 = 0.377$ GeV for $s\bar{s}$.

The meson spatial wave functions entering the above overlap integrals in the strong-decay calculations are obtained from the MGI model.

For the final states, the mixing between the strange mesons with natural parity ($L = J$) is described by

$$\begin{pmatrix} |K(nL)\rangle \\ |K'(nL)\rangle \end{pmatrix} = \begin{pmatrix} \cos\theta_{nL} & \sin\theta_{nL} \\ -\sin\theta_{nL} & \cos\theta_{nL} \end{pmatrix} \begin{pmatrix} |K(n^1L_J)\rangle \\ |K(n^3L_J)\rangle \end{pmatrix}, \quad (2.27)$$

where θ_{nL} denotes the mixing angle between the $K(n^1L_J)$ and $K(n^3L_J)$ configurations. The mixing angle for the P-wave case is taken as $\theta_{1P} = -34°$ [63], while for higher orbital excitations, it is determined by $\theta_{nL} = -\arctan\left(\sqrt{\frac{L}{L+1}}\right)$ [64].

The flavor wave functions of the isoscalar mesons are expressed in the mixing form,

$$\begin{pmatrix} X \\ X' \end{pmatrix} = \begin{pmatrix} \cos\theta_x & \sin\theta_x \\ -\sin\theta_x & \cos\theta_x \end{pmatrix} \begin{pmatrix} |n\bar{n}\rangle \\ |s\bar{s}\rangle \end{pmatrix}, \quad (2.28)$$

where X and X' denote the two isoscalar partners (e.g., η and η'), θ_x is the mixing angle in the quark-flavor basis.

TABLE II. Mass spectrum of 3^{++} states. The units of width, mass, and μ are MeV, and "Expt. inf." represents experimental information. "Br" denotes the branching ratio (in %). The three columns under "This work" correspond to varying the screening parameter μ.

$I^G n^{2S+1}L_J$ (flavor)	State	This work $\mu = 60$	This work $\mu = 78$	This work $\mu = 90$	GI [65]	Ebert [9]	Expt. inf. [1]
$1^-1^3F_3(n\bar{n})$	$a_3(2030)$	2028	1955	1904	2046	1910	$M = 1874 \pm 43 \pm 96, \Gamma = 385 \pm 121 \pm 114$[2] $M = 2031 \pm 12, \Gamma = 150 \pm 18$ [3] $\mathrm{Br}(a_3(1875) \to f_2\pi)/\mathrm{Br}(a_3(1875) \to \rho\pi) = 0.8 \pm 0.2$ [2] $\mathrm{Br}(a_3(1875) \to \rho_3(1690)\pi)/\mathrm{Br}(a_3(1875) \to \rho\pi) = 0.9 \pm 0.3$ [2]
$1^-2^3F_3(n\bar{n})$	$a_3(2275)$	2351	2234	2150	2444	2191	$M = 2275 \pm 35, \Gamma = 350^{+100}_{-50}$[4]
$1^-3^3F_3(n\bar{n})$	$a_3(3F)$	2620	2454	2333	2800	...	...
$1^-4^3F_3(n\bar{n})$	$a_3(4F)$	2849	2631	2469	3124	...	...
$0^+1^3F_3(n\bar{n})$	$f_3(2050)$	2028	1955	1904	2046	1910	$M = 2048 \pm 8, \Gamma = 213 \pm 34$ [5]
$0^+2^3F_3(n\bar{n})$	$f_3(2300)$	2351	2234	2150	2444	2191	$M = 2334 \pm 25, \Gamma = 200 \pm 20$ [6]
$0^+3^3F_3(n\bar{n})$	$f_3(3F)$	2620	2454	2333	2800	...	...
$0^+4^3F_3(n\bar{n})$	$f_3(4F)$	2849	2631	2469	3124	...	...
$0^+1^3F_3(s\bar{s})$	$f'_3(1F)$	2228	2166	2122	2234	2215	...
$0^+2^3F_3(s\bar{s})$	$f'_3(2F)$	2553	2452	2382	2623	2585	...
$0^+3^3F_3(s\bar{s})$	$f'_3(3F)$	2824	2682	2581	2972	...	...
$0^+4^3F_3(s\bar{s})$	$f'_3(4F)$	3055	2870	2736	3290	...	...

The flavor-mixing parameters for the isoscalar mesons used in this work are adopted from Ref. [34].

III. NUMERICAL RESULTS AND PHENOMENOLOGICAL ANALYSIS

The mass spectrum of the 3^{++} light meson family is calculated with the MGI model using parameters in Table I and listed in Table II. The OZI-allowed two-body strong decays are summarized in Tables III–VIII. We now turn to a phenomenological analysis of the spectrum and the decay information of the 3^{++} light meson family.

A. Mass spectra analysis

For comparison, our results are listed in Table II together with the predictions from the GI model [12], Ebert *et al.* [9], and experimental information where available. Within the MGI framework, the screening parameter μ controls the strength of color screening in the confining interaction: a larger μ corresponds to stronger screening and therefore lowers the predicted masses, with a more pronounced effect for higher radial excitations. To quantify the model dependence on μ and provide a conservative estimate of theoretical uncertainty, we vary μ in the range 60–90 MeV (i.e., $\pm 20\%$ around the nominal value $\mu = 78$ MeV used throughout this work), while keeping the other parameter values in Table I fixed. This procedure yields a mass interval for each state (Table II); notably, the sensitivity to μ increases with excitation, e.g., the spread grows from 124 MeV for the $1F$ states to 380 MeV for the $4F$ states. Such variations highlight how stronger screening (higher μ) lowers higher excitations, consistent with dynamical QCD effects such as string breaking in lattice QCD [66].

For the $1^3F_3(n\bar{n})$ states, our predictions by the MGI model show a μ dependence. As listed in Table II, varying μ from 60 to 90 MeV gives $M[a_3(2030)] \in$ 1904–2028 MeV, with the nominal value 1955 MeV at $\mu = 78$ MeV, which lies between the two experimental values of $1874 \pm 43 \pm 96$ MeV and 2031 ± 12 MeV [2,3]. Notably, the predicted interval is compatible with both experimental determinations; the weak-screening end ($\mu = 60$ MeV) moves the mass upward toward the higher

TABLE III. Total and partial decay widths of $a_3(1F)$ and $a_3(2F)$ calculated using different masses as inputs (including experimental mass and those predicted at different values of μ). "Br" denotes the branching ratio (in %); widths and μ are given in MeV. The column labeled "Expt." lists our QPC results obtained by employing the experimental mass of the initial state combined with wave functions derived at $\mu = 78$ MeV; these values do not represent measured partial widths. For brevity, channels with branching ratios below 0.5% (relative to the experimental-mass input result) are omitted.

	$a_3(2030)$									$a_3(2275)$							
	Expt.		$\mu = 78$		$\mu = 60$		$\mu = 90$			Expt.		$\mu = 78$		$\mu = 60$		$\mu = 90$	
Channel	Br	Width	Br	Width	Br	Width	Br	Width	Channel	Br	Width	Br	Width	Br	Width	Br	Width
Total	100	222	100	153	100	218	100	115	Total	100	158	100	131	100	220	100	76.9
$\pi\rho_3(1690)$	40.8	90.6	50	76.4	43.3	94.2	49.2	56.6	$\pi\rho_3(1990)$	27.9	44.2	33.3	43.8	19.4	42.7	30.8	23.7
$\pi\rho$	10.9	24.2	13.2	20.1	11.4	24.7	14.8	17	$\pi\rho_3(1690)$	11.6	18.4	10.6	13.9	9.97	22	11.4	8.78
πf_2	10.2	22.7	15.7	24	11.9	26	19.2	22.1	πf_2	7.98	12.6	8.55	11.2	6.33	14	12.3	9.49
ρh_1	8.57	19	0.997	1.52	7.55	16.4	0	0	$\pi\rho(1450)$	5.57	8.82	5.83	7.65	6.85	15.1	5.38	4.13
$\rho\omega$	7.74	17.2	7.28	11.1	7.37	16	7.17	8.23	$\pi\rho$	4.68	7.41	5.28	6.94	3.95	8.71	8.04	6.18
ηa_2	5.73	12.7	4.19	6.41	5.55	12.1	1.87	2.15	$\rho\pi(1300)$	3.77	5.96	3.4	4.47	5.18	11.4	1.25	0.958
πb_1	2.88	6.41	2.4	3.67	2.39	5.21	2.4	2.76	ρa_2	3.73	5.9	2.82	3.7	6.58	14.5	1.19	0.912
KK_2^*	2.58	5.73	0.695	1.06	2.4	5.22	0	0	$\pi f_2(1640)$	3.59	5.69	5.19	6.82	2.72	5.99	9.06	6.97
ρa_1	1.84	4.09	0	0	1.37	2.98	0	0	ρh_1	3.58	5.66	2.81	3.69	3.68	8.11	2	1.54
πf_1	1.62	3.6	1.38	2.11	1.34	2.92	1.4	1.61	ρa_1	2.76	4.36	2.04	2.68	3.88	8.54	0.871	0.67
$\pi\eta_2$	1.39	3.09	0.65	0.994	1.08	2.35	0.375	0.43	$\pi f_4(2050)$	2.73	4.32	1.58	2.08	4.06	8.95	0	0
ωb_1	1.16	2.57	0	0	0.793	1.73	0	0	$\rho\omega$	2.64	4.18	2.88	3.78	4.27	9.42	2.62	2.01
$\pi\rho(1450)$	1.13	2.51	1.02	1.55	0.8	1.74	1.12	1.29	$\pi f_0(1500)$	2.46	3.9	2.46	3.23	2.51	5.53	2.49	1.91
KK^*	0.864	1.92	0.964	1.47	0.91	1.98	0.999	1.15	$\pi f_1(2P)$	2.14	3.38	1.83	2.41	1.39	3.06	2.48	1.9
...	...	...	...	...	...	...	...	...	$\pi\rho_2(1D)$	1.93	3.05	2.09	2.74	1.77	3.91	2.55	1.96
...	...	...	...	...	...	...	...	...	ηa_2	1.86	2.94	1.47	1.94	1.46	3.21	1.57	1.21
...	...	...	...	...	...	...	...	...	$\pi b_1(2P)$	1.83	2.89	1.49	1.96	1.28	2.83	1.79	1.37
...	...	...	...	...	...	...	...	...	ωb_1	1.79	2.84	1.21	1.59	2.25	4.96	0.518	0.398
...	...	...	...	...	...	...	...	...	$\pi\rho(1900)$	0.797	1.26	0.595	0.782	0.561	1.24	0.296	0.228
...	...	...	...	...	...	...	...	...	$\pi\rho(1700)$	0.685	1.08	0.745	0.978	0.787	1.73	0.678	0.521
...	...	...	...	...	...	...	...	...	$\rho\omega(1420)$	0.678	1.07	0.144	0.19	2	4.4	0	0
...	...	...	...	...	...	...	...	...	$KK^*(1410)$	0.624	0.989	0.615	0.808	0.833	1.84	0.425	0.327
...	...	...	...	...	...	...	...	...	$\pi\eta_2$	0.576	0.913	0.634	0.833	0.738	1.63	0.564	0.434
...	...	...	...	...	...	...	...	...	$\pi b_3(2030)$	0.544	0.861	0.275	0.362	0.986	2.17	0	0

measurement around 2031 MeV, while the strong-screening endpoint ($\mu = 90$ MeV) yields a lower value being in excellent agreement with $1874 \pm 43 \pm 96$ MeV [2,3]. In comparison, the GI model (2046 MeV) is consistent with the experimental values of 2031 ± 12 and 2048 ± 8 MeV [3,5], while the relativistic quasipotential result of Ebert *et al.* (1910 MeV) agrees with the mass of $a_3(1875)$ [2] and is close to our strong-screening limit ($\mu = 90$ MeV). Similarly, we obtain $M[f_3(2050)] \in$ 1904–2028 MeV with the nominal value 1955 MeV at $\mu = 78$ MeV. The nominal mass lies about 90 MeV below the PDG average 2048 ± 8 MeV [5]. Among the scanned values, the $\mu = 60$ MeV endpoint (2028 MeV) provides the closest MGI prediction to the observed $f_3(2050)$, while the strong-screening limit gives a noticeably lower mass.

For the $2^3F_3(n\bar{n})$ states, the MGI model gives $M[a_3(2275)] = 2234$ MeV at the nominal value $\mu = 78$ MeV, which lies about 40 MeV below the experimental value 2275 ± 35 MeV for $a_3(2275)$. When varying the screening parameter in the range $\mu = 60$–90 MeV, the predicted mass spans 2150–2351 MeV. The predicted interval covers the measured mass and illustrates an enhanced μ sensitivity for the $2F$ excitation compared with the $1F$ case (a spread of 201 MeV versus 124 MeV in our $\mu = 60$–90 MeV scan). Similarly, we obtain $M[f_3(2300)] \in 2150$–2351 MeV with the nominal value 2234 MeV at $\mu = 78$ MeV, which is about 100 MeV below the experimental value 2334 ± 25 MeV [6]. Notably, the $\mu = 60$ MeV endpoint (2351 MeV) provides the closest MGI prediction to the observed $f_3(2300)$, whereas stronger screening ($\mu = 90$ MeV) yields a substantially lower mass. The GI predictions, 2444 MeV for both states, are larger than the experimental values by ∼170 and ∼110 MeV for $a_3(2275)$ and $f_3(2300)$, respectively. In contrast, the quasipotential model of Ebert *et al.* gives 2191 MeV, which is lower than the experimental values by ∼80 and ∼140 MeV, respectively. Thus for $a_3(2275)$ and $f_3(2300)$, our predictions lie between GI and Ebert *et al.*. Furthermore, once the uncertainties associated with the screening effects are taken into account, our predictions show improved agreement with the experimental data.

The predominantly $s\bar{s}$ isoscalar partners $f_3'(1F)$ and $f_3'(2F)$ are predicted to have masses of 2166 and 2452 MeV, respectively, at $\mu = 78$ MeV within the MGI framework. These values are lower than the GI values of 2234 and 2623 MeV by ∼70 and ∼170 MeV, and below the Ebert *et al.* results of 2215 and 2585 MeV by ∼50 and ∼130 MeV, respectively. By varying μ from 60 to 90 MeV, we obtain mass ranges of $M[f_3'(1F)] = 2122$–2228 MeV and $M[f_3'(2F)] = 2382$–2553 MeV. Notably, the mass of the $1F$ state approaches the GI/Ebert estimates in the weak-screening limit ($\mu = 60$ MeV), whereas the reduction remains sizable for the $2F$ excitation, reflecting the enhanced impact of screening effects on higher radial excitations.

For higher excitations, the MGI model yields systematically lower masses than the original GI model, a trend consistent with the inclusion of screening effects. As for $a_3(3F)$, our prediction is 2454 MeV, which lies ∼350 MeV below the GI value (2800 MeV). The $a_3(4F)$ has a predicted mass of 2630 MeV, which is ∼494 MeV lower than the GI result of 3124 MeV. With $\mu = 60$–90 MeV, we obtain $M[a_3(3F)] = 2333$–2620 MeV and $M[a_3(4F)] =$ 2469–2849 MeV, and the corresponding isoscalar partners $f_3(3F)$ and $f_3(4F)$ are predicted to fall within the same mass intervals with identical nominal values. Compared with the GI mass at 2800 MeV, our result for $f_3(3F)$ is 2454 MeV, lower by ∼350 MeV. The predicted mass of $f_3(4F)$ in our framework is 2630 MeV; this value represents a substantial reduction of ∼494 MeV relative to the 3124 MeV reported by the original GI model. For the predominantly $s\bar{s}$ states, we find $M[f_3'(3F)] =$ 2581–2824 MeV and $M[f_3'(4F)] = 2736$–3055 MeV, with the nominal values 2682 and 2870 MeV at $\mu = 78$ MeV, which are ∼290 and ∼420 MeV lower than the GI results of 2972 and 3290 MeV, respectively. Importantly, even in the weakest-screening case ($\mu = 60$ MeV), the $3F$ and $4F$ masses remain below the GI predictions: for example, $a_3(3F)$ and $a_3(4F)$ reach at most 2620 MeV and 2849 MeV, compared to 2800 MeV and 3124 MeV in the GI model, respectively.

In summary, the MGI model reproduces the observed $1F/2F$ levels with reasonable accuracy and predicts substantially lower masses for higher-F excitations than the GI model, as expected once color screening is included. When the uncertainty associated with μ is taken into account, the predicted mass intervals for the established $1F$ and $2F$ candidates show good agreement with experimental data, although the nominal values (at $\mu = 78$ MeV) typically deviate by approximately 50–100 MeV. The mass spectra we obtained support that $a_3(1875)$ and $a_3(2030)$ are the same state, serving as the ground state of the a_3 family, with $a_3(2275)$ as its first radial excitation, which is consistent with Ref. [7] and our previous work [8]. In addition, $f_3(2050)$ is assigned as the ground state of the f_3 family, with $f_3(2300)$ interpreted as its first radial excitation. In the next section, we will further discuss these assignments with two-body strong decay calculations. To consistently propagate the screening uncertainty, we perform these decay calculations at $\mu = 60$, 78 and 90 MeV (using the corresponding masses in Table II) and present channel-by-channel predictions for all the aforementioned states together with their μ dependence.

The present study employs the MGI model with a screened confining interaction to describe the high-L (F-wave) light-meson spectrum and to provide inputs for the $^3P_0$ decay calculations. We emphasize that, for highly excited states, unquenching effects and coupled-channel dynamics become increasingly relevant and can effectively soften the long-range confining interaction. Such a

string-breaking/screening tendency is supported by lattice studies of the static interquark potential, where the linear rise is weakened at large separations due to mixing with two-meson states [66]. In phenomenological spectroscopy, screened confining interactions have also been widely adopted in constituent quark models as an effective parametrization of these unquenching effects [67]. Explicit coupled-channel (unquenched) calculations provide concrete examples demonstrating that open-flavor thresholds can induce non-negligible mass shifts for highly excited states [68], consistent with the screening picture. Our analysis indicates that, compared with the original GI model, the screened MGI framework provides a more reasonable placement of the higher F-wave 3^{++} candidates, although residual model dependence remains for the high-lying spectrum.

On the other hand, chiral dynamics implies that pseudoscalar-meson exchange between light constituent quarks—in particular the one-pion-exchange (OPE) interaction—constitutes an important intermediate-range component of the spin-dependent force in chiral/Goldstone-boson-exchange constituent quark models [67,69–74]. Such chiral contributions are often incorporated into dynamical constituent-quark models and their extensions [68,72,75]. In the present MGI $+ {}^3P_0$ framework, these meson-exchange effects are not included explicitly; their omission should therefore be regarded as a potential source of systematic uncertainty in the description of highly excited light-meson states. A rigorous quantitative assessment would require extending the Hamiltonian with an explicit OPE term, refitting the light sector, and reevaluating both the spectrum and decay widths, which is beyond the scope of this work and is deferred to future study.

B. Strong decay analysis

We now turn to the investigation of the OZI-allowed two-body strong decays of the 3^{++} light meson family, whose results are presented in Tables III–VIII. Since decay widths are sensitive to the phase space determined by the initial-state mass, the uncertainties in the mass predictions (discussed in Sec. III A) propagate into the decay widths. Therefore, in addition to the nominal results (obtained using masses calculated at $\mu = 78$ MeV), we provide width ranges corresponding to the mass intervals derived from varying μ between 60 and 90 MeV. Furthermore, for states with experimental masses—specifically ($a_3(2030)$, $a_3(2275)$, $f_3(2050)$, and $f_3(2300)$)—we perform explicit calculations using the experimental central values (labeled as 'Expt.' in the tables). This allows us to disentangle the kinematic phase-space effects from the underlying dynamical model predictions. The $q\bar{q}$-pair creation strength $\gamma = 5.1$, introduced in Sec. II B, is applied consistently for all a_3, f_3, and f_3' states. In the decay tables, we focus on the dominant modes and omit negligible contributions by applying a cutoff of Br $< 0.5\%$. For states with experimental masses, this threshold is applied to branching ratios calculated using the observed central values. For predicted states lacking experimental counterparts, the cutoff is instead applied to branching ratios calculated using the masses obtained with our nominal screening parameter, $\mu = 78$ MeV.

1. Decay behaviors of the ground and the first excited states of the light 3^{++} meson family

As for $a_3(1F)$, we first examine the QPC result obtained by using the experimental mass ($M = 2031$ MeV) as input (the "Expt." column in Table III), which gives a total width of 222 MeV. For comparison, when the MGI masses are used, the total width ranges from 115 to 218 MeV as μ varies from 90 down to 60 MeV, with a nominal value of 153 MeV at $\mu = 78$ MeV. We note that the experimental-mass result lies slightly above the upper bound of the μ-variation band and approaches the $\mu = 60$ MeV prediction. Nevertheless, the total width obtained at $\mu = 78$ MeV is in best agreement with the experimental-width result (150 ± 18 MeV).

Using the experimental-mass input, the decay is dominated by $\pi\rho_3(1690)$, with a branching ratio of 41% and a partial width of 91 MeV. This channel remains dominant across the range $\mu = 60$–90 MeV, with partial widths varying from 57 to 94 MeV. The next most important channels are $\pi\rho$ and πf_2, with branching ratios of 11% and 10% and

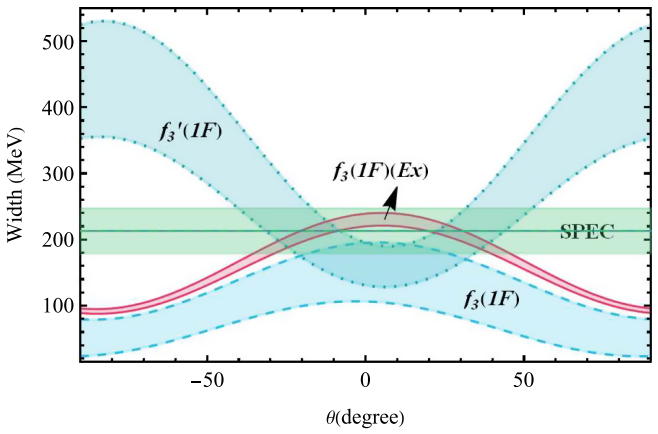


FIG. 1. The θ dependence of the total decay widths for $f_3(1F)$ and $f_3'(1F)$. The experimental width (SPEC) from Ref. [5] is represented by the horizontal green band. The region labeled $f_3(1F)$(Ex) (bounded by the two solid lines) denotes the results obtained using the experimental mass $M = 2048 \pm 8$ MeV as input. The region labeled $f_3(1F)$ (bounded by the dashed lines) represents the width range derived from the theoretical masses in the range 1904 MeV ($\mu = 90$ MeV) to 2028 MeV ($\mu = 60$ MeV). Similarly, the region labeled $f_3'(1F)$ (bounded by the dotted lines) represents the width range derived from the theoretical masses in the range 2122 MeV ($\mu = 90$ MeV) to 2228 MeV ($\mu = 60$ MeV).

partial widths of 24 MeV and 23 MeV, respectively. In particular, the ratio $\mathrm{Br}(a_3 \to \pi f_2)/\mathrm{Br}(a_3 \to \pi\rho) \simeq 0.9$, obtained with the experimental-mass input, agrees with the experimental value 0.8 ± 0.2 reported in Ref. [2] within uncertainties; using the nominal MGI input at $\mu = 78$ MeV yields a slightly larger ratio $\simeq$1.2, which remains comparable. Additionally, Ref. [2] reports $\mathrm{Br}(a_3 \to \pi\rho_3(1690))/\mathrm{Br}(a_3 \to \pi\rho) = 0.9 \pm 0.3$, whereas our calculation gives a significantly larger ratio: specifically, 3.7 with the experimental-mass input, consistently staying in the range of 3–4 for MGI masses across $\mu = 60$–90 MeV. See Table III for the remaining channels and details.

As for $a_3(2F)$, when the experimental mass ($M = 2275$ MeV) is used as input, the total width is 158 MeV. When employing the MGI mass predictions, the total width exhibits a sizable μ dependence, ranging from 77 MeV at $\mu = 90$ MeV to 220 MeV at $\mu = 60$ MeV, with a nominal value of 131 MeV at $\mu = 78$ MeV. While the experimental-mass result is well-contained within this predicted band, even the upper bound (220 MeV) remains significantly below the experimental width 350^{+100}_{-50} MeV [4].

Using the experimental-mass input, the main decay modes are $\pi\rho_3(1990)$, $\pi\rho_3(1690)$, and πf_2, with branching ratios of 28%, 12%, and 8.0%, corresponding to partial widths of 44, 18, and 13 MeV, respectively. A comparison with the μ-dependent results shows that the hierarchy of the leading channels is remarkably stable, although their absolute magnitudes scale with the available phase space; see Table III for the remaining channels and details.

Figure 1 shows the θ dependence of the total decay widths for $f_3(1F)$ and $f_3'(1F)$. To illustrate the theoretical uncertainty associated with the input mass, we vary the screening parameter μ from 60 to 90 MeV in the MGI model; the resulting width ranges are shown as shaded bands bounded by dashed lines for $f_3(1F)$ and dotted lines for $f_3'(1F)$, respectively. The horizontal green band represents the experimental range (213 ± 34 MeV) [5], while the red band (bounded by two solid lines) indicates the results obtained by using the experimental mass $M = 2048$ MeV as input for $f_3(1F)$.

For $f_3(1F)$, the total width exhibits a broad maximum around $\theta \simeq 0$ and gradually decreases as $|\theta|$ increases toward 90°. At $\theta = 0$, the widths obtained with the MGI masses span 106–195 MeV as μ varies from 90 down to 60 MeV, while using the experimental mass as input yields a central width of 232 MeV, which is consistent with the experimental band.

TABLE IV. Total and partial decay widths of $f_3(1F)$ and $f_3(2F)$ calculated using different masses as inputs (including experimental mass and those predicted at different values of μ). "Br" denotes the branching ratio (in %); widths and μ are given in MeV. The column labeled "Expt." lists our QPC results obtained by employing the experimental mass of the initial state combined with wave functions derived at $\mu = 78$ MeV; these values do not represent measured partial widths. For brevity, channels with branching ratios below 0.5% (relative to the experimental-mass input result) are omitted.

	$f_3(2050)$									$f_3(2300)$							
	Expt.		$\mu = 78$		$\mu = 60$		$\mu = 90$			Expt.		$\mu = 78$		$\mu = 60$		$\mu = 90$	
Channel	Br	Width	Br	Width	Br	Width	Br	Width	Channel	Br	Width	Br	Width	Br	Width	Br	Width
Total	100	232	100	132	100	195	100	106	Total	100	207	100	120	100	235	100	72.3
πa_2	30.3	70.4	54.3	71.7	40.7	79.4	60.9	64.8	πa_2	19.5	40.2	24.6	29.6	15.8	37.2	34.3	24.8
$\rho\rho$	16.9	39.2	17.4	23	16.9	33	16.1	17.1	$\pi a_4(2040)$	13.2	27.3	8	9.62	13.2	30.9	0.582	0.421
ρb_1	11.2	25.9	0	0	4.61	8.98	0	0	$\pi\pi_2(1880)$	10	20.7	5	6.01	8.3	19.5	1.85	1.34
ωh_1	9.48	22	0.358	0.472	7.65	14.9	0	0	$\pi a_2(1700)$	9.54	19.7	22.8	27.5	11.2	26.3	33.5	24.2
πa_1	8.1	18.8	8.04	10.6	7.17	14	7.96	8.46	$\pi a_1(1640)$	9.42	19.5	10	12.1	8.52	20	9.72	7.02
$\omega\omega$	8	18.6	8.17	10.8	7.99	15.6	7.46	7.93	ρb_1	8.57	17.7	4.34	5.22	6.67	15.7	1.88	1.36
ηf_2	6.93	16.1	7.62	10.1	7.63	14.9	5.57	5.92	$\rho\rho$	4.49	9.28	6.37	7.66	8.08	19	5.68	4.1
KK_2^*	3.1	7.2	0.806	1.06	2.68	5.22	0	0	ωh_1	4.22	8.73	2.86	3.44	3.32	7.8	1.9	1.37
$\pi\pi_2$	2.49	5.78	0.75	0.989	1.65	3.22	0.263	0.279	$\eta f_2(1640)$	4	8.27	2.98	3.59	3.94	9.25	0	0
πa_0	0.924	2.14	0.541	0.713	0.704	1.37	0.384	0.408	ηf_2	2.78	5.74	2.4	2.88	1.84	4.33	2.78	2.01
KK^*	0.888	2.06	1.12	1.47	1.02	1.98	1.08	1.15	$\rho\rho(1450)$	2.54	5.24	0	0	3.11	7.3	0	0
$\pi a_2(1700)$	0.797	1.85	0.531	0.7	0.682	1.33	0.176	0.187	$\omega\omega$	2.23	4.6	3.11	3.74	3.98	9.35	2.73	1.97
⋯	⋯	⋯	⋯	⋯	⋯	⋯	⋯	⋯	$\pi a_0(1740)$	2.19	4.52	1.39	1.67	1.96	4.6	0.796	0.575
⋯	⋯	⋯	⋯	⋯	⋯	⋯	⋯	⋯	$\omega\omega(1420)$	1.49	3.09	0.0898	0.108	1.72	4.03	0	0
⋯	⋯	⋯	⋯	⋯	⋯	⋯	⋯	⋯	$\pi\pi_2$	1.35	2.8	1.8	2.16	1.88	4.42	1.47	1.07
⋯	⋯	⋯	⋯	⋯	⋯	⋯	⋯	⋯	$\pi a_3(2030)$	0.697	1.44	0.241	0.29	0.659	1.55	0	0
⋯	⋯	⋯	⋯	⋯	⋯	⋯	⋯	⋯	$\pi a_2(2030)$	0.65	1.34	0.235	0.283	0.592	1.39	0	0
⋯	⋯	⋯	⋯	⋯	⋯	⋯	⋯	⋯	$\mathrm{K}\mathrm{K}^*(1410)$	0.64	1.32	0.672	0.808	0.781	1.84	0.452	0.327
⋯	⋯	⋯	⋯	⋯	⋯	⋯	⋯	⋯	$\eta f_0(1500)$	0.556	1.15	0.269	0.324	0.509	1.2	0.0709	0.0512

TABLE V. Total and partial decay widths of $f_3'(1F)$ and $f_3'(2F)$ calculated using masses predicted at different values of μ as inputs. "Br" denotes the branching ratio (in %); widths and μ are given in MeV. For brevity, channels with branching ratios below 0.5% (relative to the nominal-mass result predicted at $\mu = 78$ MeV) are omitted.

	$f_3'(1F)$							$f_3'(2F)$						
	$\mu = 78$		$\mu = 60$		$\mu = 90$			$\mu = 78$		$\mu = 60$		$\mu = 90$		
Channel	Br	Width	Br	Width	Br	Width	Channel	Br	Width	Br	Width	Br	Width	
Total	100	111	100	195	100	131	Total	100	145	100	284	100	84	
KK_2^*	46.2	51.4	38.9	76	50.2	65.8	KK_2^*	21.4	31.2	13.1	37.1	31.6	26.5	
KK^*	22.9	25.5	21.2	41.4	24	31.4	$K^*K^*(1410)$	12.2	17.7	14.8	42	6.8	5.71	
K^*K^*	15.3	17.1	15.9	31	14.4	18.9	KK^*	11.5	16.7	6.18	17.6	18.4	15.5	
$\eta f_2'(1525)$	5.78	6.43	8.33	16.3	3	3.93	$KK_3^*(1780)$	9.61	14	9.47	26.9	5.01	4.2	
KK_1'	4.08	4.54	5.02	9.8	3.2	4.19	$KK^*(1410)$	7.28	10.6	5.57	15.8	8.97	7.53	
$KK^*(1410)$	3.43	3.82	2.61	5.1	3.85	5.04	K^*K_1	6.68	9.73	4.58	13	7.66	6.43	
$\phi\phi$	1.25	1.4	2.37	4.63	0.575	0.752	$KK_1'(2P)$	4.93	7.17	4.36	12.4	3.61	3.03	
⋯	⋯	⋯	⋯	⋯	⋯	⋯	$K^*K(1460)$	4.84	7.04	5.72	16.3	0.813	0.682	
⋯	⋯	⋯	⋯	⋯	⋯	⋯	$K^*K_2^*$	4.48	6.52	7.09	20.2	2.78	2.33	
⋯	⋯	⋯	⋯	⋯	⋯	⋯	K^*K^*	4.48	6.51	2.74	7.8	6.68	5.61	
⋯	⋯	⋯	⋯	⋯	⋯	⋯	$KK_2^*(1980)$	3.13	4.55	11.7	33.2	0	0	
⋯	⋯	⋯	⋯	⋯	⋯	⋯	$KK_2(1820)$	2.65	3.86	2.66	7.57	1.45	1.22	
⋯	⋯	⋯	⋯	⋯	⋯	⋯	K^*K_1'	1.04	1.51	3.27	9.3	1.02	0.855	
⋯	⋯	⋯	⋯	⋯	⋯	⋯	$\eta f_2'(1525)$	0.99	1.44	0.777	2.21	1.24	1.04	
⋯	⋯	⋯	⋯	⋯	⋯	⋯	$KK_1(1790)$	0.89	1.29	1.39	3.95	0.332	0.279	
⋯	⋯	⋯	⋯	⋯	⋯	⋯	$KK^*(1680)$	0.856	1.25	0.496	1.41	1.14	0.955	
⋯	⋯	⋯	⋯	⋯	⋯	⋯	KK_1	0.747	1.09	0.434	1.23	1.05	0.88	
⋯	⋯	⋯	⋯	⋯	⋯	⋯	$K^*K_0^*(1430)$	0.72	1.05	1.03	2.93	0.188	0.158	
⋯	⋯	⋯	⋯	⋯	⋯	⋯	$\phi\phi$	0.631	0.919	0.98	2.79	0.545	0.457	

Taking the experimental mass as input, the calculated width overlaps the experimental (SPEC) band [5] over the angular interval about $-34° \lesssim \theta \lesssim 42°$. For $\mu = 60$ MeV, the overlap region covers $-20° \lesssim \theta \lesssim 25°$, where the width at $\theta \simeq 4°$ is closest to the experimental central value [5]. Reference [11] reports $\theta_{1^3F_3} = 3 \pm 2°$, which is numerically consistent with our representative choice and lies within the same overlap region. Regarding $f_3'(1F)$, the variation is opposite in phase: a pronounced minimum occurs near $\theta \simeq 0$, and the width increases as $|\theta| \to 90°$.

Numerically, when we take $\theta = 0$ and use the experimental mass as input, $f_3(1F)$ has a total decay width of 232 MeV (Table IV). The main decay channels are πa_2, $\rho\rho$, and ρb_1, with branching ratios of 30%, 17%, and 11%, corresponding to partial widths of 70, 39, and 26 MeV, respectively. For comparison, when the MGI masses are used, the total width is reduced to 106–195 MeV for $\mu = 90$–60 MeV (with a nominal value of 132 MeV at $\mu = 78$ MeV). In particular, certain channels that are important under the experimental-mass input become strongly suppressed or even kinematically closed for smaller MGI masses (e.g., ρb_1 vanishes at $\mu = 78$ and 90 MeV), which reduces the total width and alters the branching pattern. The remaining channels and detailed decay information are summarized in Table IV.

According to Table V, we obtain the decay width of 111–195 MeV (with the nominal value of 111 MeV) for

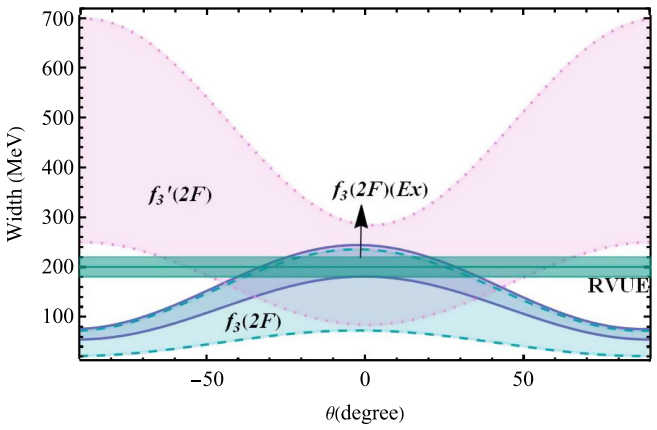


FIG. 2. The θ dependence of the total decay widths of $f_3(2F)$ and $f_3'(2F)$. The experimental width (RVUE) from Ref. [6] is represented by the horizontal green band. The region labeled $f_3(2F)$(Ex) (bounded by the two solid lines) denotes the results obtained using the experimental mass $M = 2334 \pm 25$ MeV as input. The region labeled $f_3(2F)$ (bounded by the dashed lines) represents the width range derived from the theoretical masses in the range 2150 MeV ($\mu = 90$ MeV) to 2351 MeV ($\mu = 60$ MeV). Similarly, the region labeled $f_3'(2F)$ (bounded by the dotted lines) represents the width range derived from the theoretical masses in the range 2382 MeV ($\mu = 90$ MeV) to 2553 MeV ($\mu = 60$ MeV).

TABLE VI. Total and partial decay widths of $a_3(3F)$ and $a_3(4F)$ calculated using masses predicted at different values of μ as inputs. "Br" denotes the branching ratio (in %); widths and μ are given in MeV. For brevity, channels with branching ratios below 0.5% (relative to the nominal-mass result predicted at $\mu = 78$ MeV) are omitted.

	$a_3(3F)$							$a_3(4F)$					
	$\mu = 78$		$\mu = 60$		$\mu = 90$			$\mu = 78$		$\mu = 60$		$\mu = 90$	
Channel	Br	Width	Br	Width	Br	Width	Channel	Br	Width	Br	Width	Br	Width
Total	100	111	100	241	100	44.4	Total	100	78.8	100	263	100	33.8
$\pi\rho_3(2250)$	24.8	27.5	7.32	17.7	0	0	$\pi\rho_3(2250)$	10.3	8.09	3.32	8.73	5.08	1.72
$\pi\rho_3(1990)$	11	12.2	7.53	18.2	12.4	5.53	$\pi\rho_3(1990)$	9.13	7.19	5.73	15	8.1	2.74
$\pi f_2(1640)$	5.85	6.48	3.75	9.05	11.3	5	$\pi f_2(1640)$	6.2	4.88	2.76	7.24	9.92	3.35
$\pi\rho_3(1690)$	4.8	5.31	4.07	9.82	6.71	2.98	$\pi f_2(4\mathrm{P})$	4.08	3.22	1.81	4.75	5.3	1.79
$\pi\rho$	4.39	4.86	3.14	7.58	7.93	3.52	$\pi\rho$	3.89	3.06	1.4	3.68	6.88	2.33
$\rho\omega$	4.09	4.53	3.59	8.65	5.2	2.31	$\rho\omega$	3.14	2.47	0.982	2.58	4.9	1.66
πf_2	3.81	4.22	2.03	4.9	8.35	3.71	$\pi f_2(1950)$	3.13	2.47	0.953	2.5	7.35	2.49
$\pi\rho(1450)$	3.13	3.46	1.55	3.74	6.24	2.77	$\pi\rho(1450)$	2.88	2.27	2.09	5.48	4.75	1.61
$\pi f_2(1950)$	2.89	3.2	1.8	4.34	7.48	3.32	$\pi\rho(1900)$	2.8	2.21	1.09	2.87	3.29	1.11
$\pi\rho(1900)$	2.87	3.18	4.7	11.3	1.69	0.75	ρa_2	2.57	2.02	2.01	5.27	2.38	0.806
ρa_2	2.69	2.97	3.59	8.65	2.58	1.14	πf_2	2.21	1.74	0.796	2.09	4.81	1.63
ρa_1	2.18	2.41	2.14	5.16	2.4	1.07	$\pi\rho_3(1690)$	2.13	1.67	1.03	2.71	3.29	1.11
$\pi\rho_2(2D)$	1.99	2.2	1.57	3.8	2.7	1.2	$\rho\omega(1420)$	2.07	1.63	3.19	8.38	0.85	0.287
$\rho\pi(1300)$	1.91	2.11	1.66	4.01	2.76	1.22	$\pi\rho(4\mathrm{S})$	2.02	1.59	3.75	9.86	0.185	0.0627
ρh_1	1.73	1.92	1.58	3.81	2.33	1.04	$\rho\pi(1300)$	1.99	1.57	1.92	5.05	2.22	0.751
$\pi b_1(1960)$	1.55	1.72	2.17	5.24	0.758	0.337	$\pi\rho_2(2D)$	1.86	1.47	0.822	2.16	2.79	0.945
$\pi\rho_2(1D)$	1.43	1.58	0.876	2.11	2.67	1.19	$\pi\rho_2(3D)$	1.75	1.38	1.17	3.07	1.49	0.503
$\pi f_3(2050)$	1.32	1.46	0.147	0.356	0.019	0.00842	$\rho\pi_2$	1.62	1.27	1.08	2.83	0.218	0.0736
$\pi f_0(1500)$	1.24	1.37	0.745	1.8	2.32	1.03	ρa_1	1.58	1.24	0.76	2	2.11	0.715
$\pi f_1(3\mathrm{P})$	1.11	1.23	0.767	1.85	1.69	0.749	$\omega\rho(1450)$	1.45	1.14	2.46	6.47	0.501	0.17
ωb_1	0.893	0.989	0.981	2.37	1.01	0.449	$\pi\rho_2(1D)$	1.36	1.07	0.662	1.74	2.2	0.745
πf_1	0.851	0.942	0.697	1.68	1.14	0.508	ρh_1	1.33	1.05	0.719	1.89	1.74	0.588
$\pi\eta_2$	0.82	0.908	0.66	1.59	1.17	0.518	$\pi b_1(1960)$	1.32	1.04	1.11	2.92	1.25	0.424
$\rho\omega(1420)$	0.798	0.884	2.69	6.49	0.149	0.0661	$\eta a_2(1950)$	1.24	0.974	1.46	3.85	0	0
$\pi f_4(2300)$	0.738	0.817	4.5	10.8	0	0	$\pi f_3(2300)$	1.2	0.948	0.226	0.594	0	0
$\pi\rho(1700)$	0.677	0.75	0.554	1.34	0.908	0.403	$\pi\rho(2000)$	1.16	0.911	0.598	1.57	1.07	0.361
$\pi\rho(4\mathrm{S})$	0.632	0.699	0.704	1.7	0.0177	0.00785	$\rho h_1(1595)$	1.14	0.898	1.87	4.9	0.468	0.158
$\pi\rho(2000)$	0.625	0.692	0.391	0.942	0.649	0.288	$\rho a_1(1640)$	1.12	0.884	2.23	5.86	0.458	0.155
$\pi f_4(2050)$	0.608	0.673	1.19	2.87	0.215	0.0954	$\pi\rho_3(2G)$	1.05	0.829	0.361	0.949	1.56	0.529
$\pi\rho_3(1G)$	0.573	0.634	0.317	0.764	1.11	0.494	πf_1	1.05	0.826	0.486	1.28	1.51	0.511
$KK_3^*(1780)$	0.539	0.596	0.38	0.918	0.812	0.361	$\pi b_3(2244)$	1.03	0.811	1.15	3.02	0.221	0.0749
ηa_1	0.536	0.593	0.444	1.07	0.723	0.321	$\rho a_2(1700)$	1.01	0.795	2.84	7.47	0	0
$\pi b_3(2244)$	0.513	0.568	1.44	3.46	0	0	$\pi f_4(3F)$	0.965	0.76	1.5	3.94	0	0
$\eta a_2(1700)$	0.505	0.558	1.25	3.02	0.00484	0.00215	$\pi f_4(2300)$	0.883	0.696	2.04	5.35	0.0108	0.00365
⋯	⋯	⋯	⋯	⋯	⋯	⋯	$\pi\eta_2$	0.794	0.626	0.396	1.04	1.14	0.385
⋯	⋯	⋯	⋯	⋯	⋯	⋯	ωb_1	0.762	0.6	0.468	1.23	0.845	0.286
⋯	⋯	⋯	⋯	⋯	⋯	⋯	$\pi b_1(2240)$	0.757	0.596	0.986	2.59	0.0312	0.0106
⋯	⋯	⋯	⋯	⋯	⋯	⋯	$\pi f_3(2050)$	0.703	0.554	0.0974	0.256	0.0341	0.0115
⋯	⋯	⋯	⋯	⋯	⋯	⋯	$\pi f_1(4\mathrm{P})$	0.701	0.552	0.419	1.1	0.555	0.188
⋯	⋯	⋯	⋯	⋯	⋯	⋯	$\rho\omega_2(1D)$	0.63	0.496	0.354	0.929	0.625	0.212
⋯	⋯	⋯	⋯	⋯	⋯	⋯	$\omega\rho_2(1D)$	0.613	0.483	0.356	0.936	0.557	0.189
⋯	⋯	⋯	⋯	⋯	⋯	⋯	$\pi\eta_2(2D)$	0.602	0.474	0.348	0.915	0.664	0.225
⋯	⋯	⋯	⋯	⋯	⋯	⋯	$\pi\rho(3\mathrm{D})$	0.536	0.422	0.385	1.01	0.343	0.116
⋯	⋯	⋯	⋯	⋯	⋯	⋯	πb_1	0.534	0.42	0.235	0.618	0.691	0.234
⋯	⋯	⋯	⋯	⋯	⋯	⋯	$\eta a_1(1640)$	0.522	0.411	0.331	0.87	0.414	0.14
⋯	⋯	⋯	⋯	⋯	⋯	⋯	ηa_1	0.519	0.409	0.237	0.621	0.764	0.258
⋯	⋯	⋯	⋯	⋯	⋯	⋯	$\rho\omega_3(1670)$	0.519	0.408	0.561	1.47	0.0409	0.0138
⋯	⋯	⋯	⋯	⋯	⋯	⋯	$\pi f_1(2P)$	0.512	0.403	0.46	1.21	0.209	0.0708

$f_3'(1F)$ at $\theta = 0$. Across the scanned μ range, KK_2^* remains the dominant channel; specifically in the nominal case, it contributes 46% of the branching ratio and 51 MeV of the partial width. KK^* provides 23% of the branching ratio with a partial width of 26 MeV, while K^*K^* accounts for 15% with 17 MeV.

The total decay widths of $f_3(2F)$ and $f_3'(2F)$ as functions of the flavor-mixing angle θ are shown in Fig. 2. To illustrate the theoretical uncertainty associated with the input mass, the parameter μ is varied from 60 to 90 MeV in the MGI model; the resulting width ranges are shown as shaded bands bounded by dashed lines for $f_3(2F)$ and dotted lines for $f_3'(2F)$, respectively. Additionally, the results obtained by employing the experimental mass of $f_3(2300)$ ($M = 2334$ MeV) as input are depicted by the purple band (bounded by solid lines). The experimental width (200 ± 20 MeV) [6] is indicated by the horizontal green band.

For the $f_3(2F)$ case, the total width exhibits a bell-shaped behavior, peaking near $\theta \simeq 0$ and decreases as $|\theta| \to 90°$. When the experimental mass is adopted, the predicted width at $\theta = 0$ is 207^{+37}_{-26} MeV, which is in excellent agreement with the experimental value of 200 ± 20 MeV. Opposite to $f_3(2F)$, $f_3'(2F)$ exhibits a minimum near $\theta = 0$ and increases progressively as $|\theta| \to 90°$.

According to Table IV, the total width of $f_3(2F)$ at $\theta = 0$ ranges from 72 to 235 MeV (with a nominal value of 120 MeV at $\mu = 78$ MeV). Taking the experimental mass as input, most of the branching ratio is carried by πa_2, contributing 20% of the width and a partial width of 40 MeV. $\pi a_4(2040)$ accounts for 13% and 27 MeV, while $\pi\pi_2(1880)$ adds 10% and 21 MeV. Table IV summarizes all other decay modes. Notably, the result obtained using the experimental mass is consistent with the prediction at the weak-screening limit ($\mu = 60$ MeV).

The calculated total width for $f_3'(2F)$ is about 84–284 MeV (with a nominal value of 145 MeV at $\mu = 78$ MeV) when we take $\theta = 0$. Ordering channels by yield for $\mu = 78$ MeV, KK_2^* supplies 21% of the branching ratio with a 31 MeV partial width, $K^*K^*(1410)$ supplies 12% and 18 MeV, and KK^* supplies 12% and 17 MeV. The complete set of other channels is given in Table V.

2. Predictions of the second and the third excited states of the light 3^{++} meson family

We predict a total width of 44–241 MeV (with a nominal value of 111 MeV at $\mu = 78$ MeV) for $a_3(3F)$. The pronounced uncertainty reflects the significant mass shift (~290 MeV) occurring between the $\mu = 60$ and $\mu = 90$ MeV scenarios. The specific decay channels and their associated details are given in Table VI. The four leading modes at $\mu = 78$ MeV are $\pi\rho_3(2250)$ with a branching ratio of 25% and a partial width of 28 MeV, $\pi\rho_3(1990)$ with 11% and 12 MeV, $\pi f_2(1640)$ with 6% and 6 MeV, and $\pi\rho_3(1690)$ with 5% and 5 MeV, respectively.

For the $a_3(4F)$ state, we obtain a total width of 34–263 MeV (with a nominal value of 79 MeV at $\mu = 78$ MeV). The main decay modes are $\pi\rho_3(2250)$ with 10% and 8 MeV, then $\pi\rho_3(1990)$ with 9% and 7 MeV, followed by $\pi f_2(1640)$ with 6% and 5 MeV, and $\pi f_2(4P)$ with 4% and 3 MeV, for $\mu = 78$ MeV. Remaining channels and details are given in Table VI.

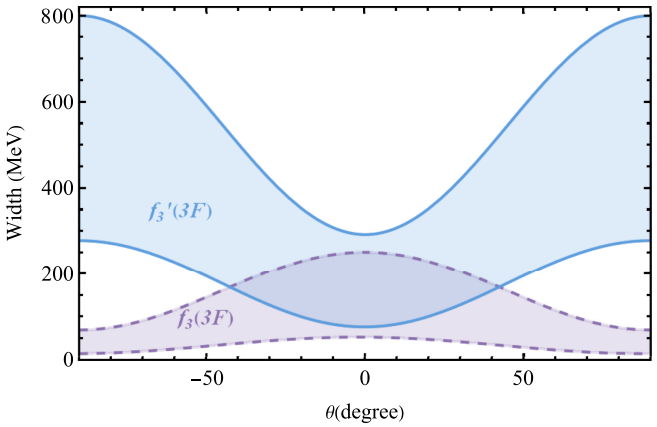


FIG. 3. The θ dependence of the total decay widths of $f_3(3F)$ and $f_3'(3F)$. The region labeled $f_3(3F)$ (bounded by the two dashed lines) represents the width range derived from the theoretical masses in the range 2333 MeV ($\mu = 90$ MeV) to 2620 MeV ($\mu = 60$ MeV). Similarly, the region labeled $f_3'(3F)$ (bounded by the two solid lines) represents the width range derived from the theoretical masses in the range 2581 MeV ($\mu = 90$ MeV) to 2824 MeV ($\mu = 60$ MeV).

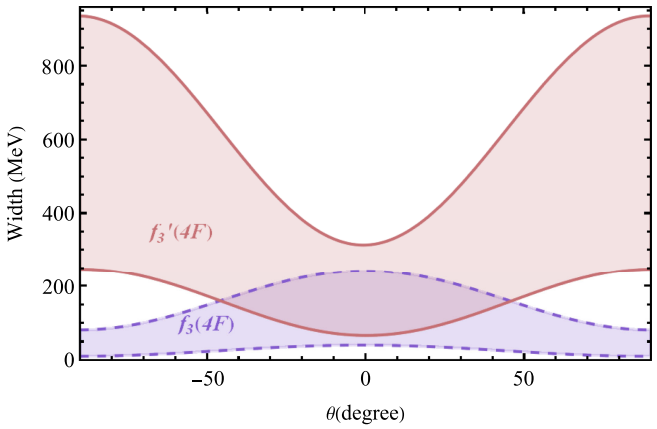


FIG. 4. The θ dependence of the total decay widths for $f_3(4F)$ and $f_3'(4F)$. The region labeled $f_3(4F)$ (bounded by the two dashed lines) represents the width range derived from the theoretical masses in the range 2469 MeV ($\mu = 90$ MeV) to 2849 MeV ($\mu = 60$ MeV). Similarly, the region labeled $f_3'(4F)$ (bounded by the two solid lines) represents the width range derived from the theoretical masses in the range 2736 MeV ($\mu = 90$ MeV) to 3055 MeV ($\mu = 60$ MeV).

TABLE VII. Total and partial decay widths of $f_3(3F)$ and $f_3(4F)$ calculated using masses predicted at different values of μ as inputs. "Br" denotes the branching ratio (in %); widths and μ are given in MeV. For brevity, channels with branching ratios below 0.5% (relative to the nominal-mass result predicted at $\mu = 78$ MeV) are omitted.

	$f_3(3F)$							$f_3(4F)$					
	$\mu = 78$		$\mu = 60$		$\mu = 90$			$\mu = 78$		$\mu = 60$		$\mu = 90$	
Channel	Br	Width	Br	Width	Br	Width	Channel	Br	Width	Br	Width	Br	Width
Total	100	96.7	100	250	100	52.5	Total	100	75.4	100	241	100	40.2
$\pi a_2(1700)$	19.5	18.8	11.1	27.8	25.1	13.2	$\pi a_2(1700)$	14	10.6	6.91	16.7	17.3	6.96
πa_2	10.5	10.1	4.76	11.9	16.9	8.89	$\pi a_2(1950)$	10.2	7.71	3.27	7.9	18.8	7.58
$\pi a_4(2255)$	10.4	10	14	35	0	0	$\pi a_2(2175)$	8.05	6.07	9.39	22.7	14.5	5.83
$\pi a_2(1950)$	10.1	9.81	5.05	12.7	19.5	10.2	$\pi a_4(2255)$	7.08	5.34	8.39	20.3	0.703	0.283
$\rho\rho$	9.57	9.26	7.06	17.7	9	4.72	$\rho\rho$	6.76	5.1	2.21	5.35	8.47	3.41
$\omega\omega$	4.58	4.43	3.38	8.46	4.3	2.26	πa_2	5.3	4	2.06	4.98	9.23	3.71
$\pi a_1(3P)$	3.82	3.69	2.22	5.55	4.28	2.25	$\rho\rho(1450)$	4.78	3.61	8.34	20.1	1.37	0.551
πa_1	3.48	3.36	2.45	6.13	3.34	1.75	πa_1	4.43	3.34	2.21	5.33	4.96	1.99
ρb_1	3.27	3.16	2.96	7.43	2.77	1.46	$\omega\omega$	3.18	2.4	1.03	2.49	4	1.61
$\pi a_4(2040)$	3.21	3.11	4.29	10.7	1.19	0.623	$\pi a_4(3F)$	3.02	2.28	4.9	11.8	0	0
$\eta f_2(1640)$	2.58	2.49	2.08	5.22	1.47	0.77	ρb_1	2.5	1.89	1.58	3.82	2.27	0.912
$\pi\pi_2$	2.24	2.17	1.61	4.03	2.24	1.18	$\pi\pi_2(1880)$	2.43	1.84	1.6	3.87	1.9	0.764
ωh_1	1.87	1.81	1.46	3.67	1.83	0.961	$\pi a_1(4P)$	2.2	1.66	1.37	3.3	1.4	0.563
$\rho\rho(1450)$	1.82	1.76	7.37	18.5	0.0693	0.0364	$\omega\omega(1420)$	2.08	1.57	3.38	8.15	0.669	0.269
$\pi\pi_2(1880)$	1.71	1.65	2.3	5.77	0.739	0.388	$\rho\rho_2(1D)$	1.97	1.49	1.15	2.79	1.58	0.635
$\pi a_2(2175)$	1.23	1.19	0.943	2.36	0.587	0.308	$\pi\pi_2$	1.84	1.39	0.989	2.39	2.07	0.833
$\pi a_2(2F)$	1.13	1.1	0.734	1.84	1.02	0.534	$\eta f_2(1640)$	1.62	1.22	1.07	2.6	1.26	0.506
$\rho\rho_2(1D)$	1.11	1.07	1.76	4.42	0	0	$\rho b_1(2P)$	1.54	1.16	1.22	2.95	0.888	0.357
$\omega\omega(1420)$	0.864	0.836	2.59	6.48	0.0994	0.0522	$\eta f_2(1950)$	1.46	1.1	1.6	3.86	0	0
$\pi a_0(3P)$	0.854	0.826	0.621	1.56	0.644	0.338	ωh_1	1.32	0.997	0.753	1.82	1.37	0.551
ηf_2	0.809	0.782	0.448	1.12	1.13	0.593	$\rho\rho_3(1690)$	1.28	0.967	1.74	4.19	0.0118	0.00474
$KK_3^*(1780)$	0.617	0.596	0.366	0.918	0.687	0.361	$\pi a_4(2040)$	1.17	0.886	1.65	3.99	0.428	0.172
$\pi a_1(1640)$	0.572	0.553	0.447	1.12	0.627	0.329	$\omega h_1(1595)$	1.08	0.812	1.95	4.7	0.399	0.16
...	...	...	...	...	...	...	$\pi a_2(3F)$	0.9	0.679	0.691	1.67	0.0808	0.0325
...	...	...	...	...	...	...	$\pi a_1(1640)$	0.641	0.483	0.425	1.03	0.287	0.115
...	...	...	...	...	...	...	$\omega\omega_2(1D)$	0.64	0.483	0.388	0.936	0.469	0.189
...	...	...	...	...	...	...	$\pi a_3(3F)$	0.552	0.416	0.562	1.36	0	0
...	...	...	...	...	...	...	$\pi a_0(3P)$	0.518	0.391	0.0661	0.159	1.28	0.515
...	...	...	...	...	...	...	$\omega\omega_3(1670)$	0.51	0.385	0.603	1.46	0.0201	0.0081

TABLE VIII. Total and partial decay widths of $f_3'(3F)$ and $f_3'(4F)$ calculated using masses predicted at different values of μ as inputs. "Br" denotes the branching ratio (in %); widths and μ are given in MeV. For brevity, channels with branching ratios below 0.5% (relative to the nominal-mass result predicted at $\mu = 78$ MeV) are omitted.

	$f_3'(3F)$							$f_3'(4F)$					
	$\mu = 78$		$\mu = 60$		$\mu = 90$			$\mu = 78$		$\mu = 60$		$\mu = 90$	
Channel	Br	Width	Br	Width	Br	Width	Channel	Br	Width	Br	Width	Br	Width
Total	100	127	100	292	100	76	Total	100	129	100	313	100	66.3
KK_2^*	13.7	17.4	7.22	21.1	18.8	14.3	KK_2^*	8.26	10.7	4.16	13	12.8	8.52
$KK_3^*(1780)$	9.25	11.8	6.57	19.2	7.84	5.96	$KK_3^*(1780)$	6.78	8.75	4.58	14.3	7.06	4.68
$KK_2^*(1980)$	8.46	10.8	6.67	19.5	3.86	2.93	$KK_2^*(3P)$	6.15	7.94	3.88	12.1	6.08	4.03
KK^*	7.6	9.66	3.73	10.9	11.4	8.7	$K^*K_2^*$	6.04	7.8	5.09	15.9	5.22	3.46
$KK^*(1410)$	7.6	9.66	4.51	13.2	9.75	7.41	$KK_2^*(1980)$	5.87	7.58	4	12.5	4.88	3.24
$K^*K_2^*$	5.84	7.43	5.52	16.1	3.98	3.02	KK^*	5.39	6.96	2.89	9.03	8.65	5.74
K^*K_1	5.71	7.26	3.24	9.45	6.86	5.22	$KK^*(1410)$	4.89	6.32	2.44	7.64	7.68	5.1
$K^*K^*(1410)$	5.58	7.09	3.38	9.87	6.56	4.99	$KK_3^*(2D)$	4.58	5.91	3.49	10.9	3.68	2.44

(Table continued)

TABLE VIII. *(Continued)*

	$f_3'(3F)$							$f_3'(4F)$					
	$\mu = 78$		$\mu = 60$		$\mu = 90$			$\mu = 78$		$\mu = 60$		$\mu = 90$	
Channel	Br	Width	Br	Width	Br	Width	Channel	Br	Width	Br	Width	Br	Width
K^*K^*	4.48	5.69	3.17	9.24	5.3	4.03	K^*K^*	4.46	5.75	3.23	10.1	5.46	3.62
$KK^*(3S)$	4.39	5.58	3.22	9.39	3.35	2.55	K^*K_1	4.1	5.29	2.31	7.24	5.67	3.76
$K^*\mathrm{K}(1460)$	4.29	5.45	2.41	7.02	4.18	3.18	$KK^*(3S)$	3.23	4.16	2.03	6.36	4.16	2.76
$KK_2{}'(2D)$	3.63	4.62	3.09	9.01	0.143	0.109	$K^*K^*(1410)$	3.03	3.91	1.17	3.66	4.93	3.27
K^*K_1'	2.83	3.6	3.1	9.06	1.43	1.09	K^*K_1'	2.98	3.85	2.61	8.16	2.34	1.55
$KK_2(1820)$	2.25	2.86	1.46	4.26	2.14	1.63	$K^*\mathrm{K}(1460)$	2.87	3.7	1.37	4.28	3.88	2.57
$KK_3{}^*(2D)$	1.84	2.34	2.29	6.67	6.42	4.88	$KK_4{}^*(2045)$	2.68	3.47	3.15	9.87	0.421	0.279
$KK_1{}'(3\mathrm{P})$	1.47	1.87	3.42	9.98	0	0	$K_1K_2{}^*$	2.56	3.31	0.61	1.91	0.308	0.204
$KK_4{}^*(2045)$	1.37	1.74	4.13	12	0.746	0.568	$KK^*(4S)$	2.41	3.11	2.02	6.31	0	0
KK_1'	1.26	1.6	0.781	2.28	1.63	1.24	$KK_2{}'(2D)$	2.22	2.87	1.48	4.62	2.11	1.4
$K^*K_1{}'(2P)$	1.15	1.46	2.4	6.99	0	0	$KK_2(1820)$	1.92	2.48	1.18	3.68	2.21	1.47
$K^*K_0{}^*(1430)$	0.857	1.09	0.708	2.06	0.611	0.465	KK_1'	1.74	2.25	1.1	3.45	2.38	1.58
$\phi\phi$	0.802	1.02	0.678	1.98	0.72	0.548	$K^*K_2(1820)$	1.7	2.2	0.613	1.92	0.111	0.0733
$KK_1(1790)$	0.796	1.01	0.89	2.6	0.44	0.334	$K^*\mathrm{K}(1830)$	1.66	2.14	1.51	4.71	0.00012	0.0000796
$KK^*(1680)$	0.659	0.838	0.344	1	0.868	0.66	$K^*K_1{}'(2P)$	1.13	1.46	2.33	7.3	0.571	0.378
$KK_1{}^*(2D)$	0.594	0.755	0.491	1.43	0.278	0.212	$K^*K_1(1790)$	1.09	1.4	3.51	11	0.679	0.45
⋯	⋯	⋯	⋯	⋯	⋯	⋯	⋯	$KK_4{}^*(2F)$	0.966	1.25	0.25	0.782	0	0
⋯	⋯	⋯	⋯	⋯	⋯	⋯	⋯	$K^*K_3{}^*(1780)$	0.96	1.24	1.59	4.96	0.295	0.196
⋯	⋯	⋯	⋯	⋯	⋯	⋯	⋯	$K_1K^*(1410)$	0.717	0.926	2.71	8.48	1.11	0.736
⋯	⋯	⋯	⋯	⋯	⋯	⋯	⋯	$KK_2(2250)$	0.681	0.88	1.24	3.87	0	0
⋯	⋯	⋯	⋯	⋯	⋯	⋯	⋯	$K^*K_0{}^*(1430)$	0.636	0.822	0.458	1.43	0.624	0.414
⋯	⋯	⋯	⋯	⋯	⋯	⋯	⋯	$KK_1{}^*(2D)$	0.612	0.79	0.341	1.07	0.763	0.506
⋯	⋯	⋯	⋯	⋯	⋯	⋯	⋯	$KK_3'(1F)$	0.583	0.753	0.811	2.54	0.0949	0.0629
⋯	⋯	⋯	⋯	⋯	⋯	⋯	⋯	$K^*K_2(1770)$	0.52	0.672	0.171	0.537	0.203	0.135

Figures 3 and 4 display the total widths of $f_3(3F)$, $f_3'(3F)$, $f_3(4F)$, and $f_3'(4F)$ as functions of the flavor-mixing angle θ obtained with different mass as inputs. The resulting bands illustrate the pronounced sensitivity of these high-excitation widths to the screening parameter μ. $f_3(3F)$ and $f_3(4F)$ bands show a broad maximum near $\theta \simeq 0$ and then decrease monotonically as $|\theta| \to 90°$. In contrast, the $f_3'(3F)$ and $f_3'(4F)$ display an opposite trend, reaching a clear minimum around $\theta \simeq 0$ and increasing sharply toward the boundaries.

Regarding the $f_3(3F)$ state, the calculated total decay width ranges from 53 to 250 MeV (with a nominal value of 97 MeV at $\mu = 78$ MeV) at $\theta = 0$. The main decay mode is $\pi a_2(1700)$ with a branching ratio of 20% and a partial width of 19 MeV. While πa_2, $\pi a_4(2255)$, and $\pi a_2(1950)$ modes each contribute 10% to the total width with the partial width about 10 MeV. The $\rho\rho$, $\omega\omega$, $\pi a_1(3P)$, and πa_1 channels remain important contributors. The rest of the channels, together with specifics, are listed in Table VII.

In the hidden-strangeness sector, $f_3'(3F)$ has a total width of 76–292 MeV (with a nominal value of 127 MeV) at $\theta = 0$. Table VIII lists the specific decay channels and the related decay information, among which KK_2^* contributes 14% with a partial width of 17 MeV, $KK_3^*(1780)$ contributes 9% with 12 MeV, and $KK_2^*(1980)$ contributes 8% with 11 MeV. Additionally, the KK^*, $KK^*(1410)$, $K^*K_2^*$, and K^*K_1 modes serve as further noteworthy decay components.

As for $f_3(4F)$, the predicted width is about 40–241 MeV (with a nominal value of 75 MeV at $\mu = 78$ MeV) at $\theta = 0$. The primary decay mode is $\pi a_2(1700)$, with a branching ratio of 14% and a partial width of 11 MeV. Other significant contributors include $\pi a_2(1950)$, $\pi a_2(2175)$, and $\pi a_4(2255)$, accounting for branching fractions of 10%, 8%, and 7%, and partial widths of 8 MeV, 6 MeV, and 5 MeV, respectively. Other notable contributions arise from $\rho\rho$, πa_2, $\rho\rho(1450)$, and πa_1. See Table VII for other channels.

Finally, for $f_3'(4F)$, we obtain a total width ranging from 66 to 313 MeV (with a nominal value of 129 MeV) at $\theta = 0$. The four main strange final states are KK_2^* with a branching ratio of 8% and a partial width of 11 MeV, followed by $KK_3^*(1780)$ (7%, 9 MeV), $KK_2^*(3\mathrm{P})$ (6%, 8 MeV), and $K^*K_2^*$ (6%, 8 MeV). Further sizable contributions come from $KK_2^*(1980)$, KK^*, $KK^*(1410)$, and $KK_3^*(2D)$, as tabulated in Table VIII.

IV. CONCLUSION

In this work, we systematically studied the mass spectrum and OZI-allowed two-body strong decays of the 3^{++}

family within the MGI model combined with the QPC model. Based on our numerical results, we discussed possible assignments for the observed $a_3(1875)$, $a_3(2030)$, $a_3(2275)$, $f_3(2050)$, and $f_3(2300)$ states, while providing theoretical predictions for the as-yet-unobserved higher excitations.

Our analysis indicates that $a_3(1875)$ and $a_3(2030)$ likely correspond to the same state, specifically the a_3 ground state, while $f_3(2050)$ is identified as the ground state of the f_3 family. Regarding the first radial excitations, $a_3(2275)$ and $f_3(2300)$ can be interpreted as the $a_3(2F)$ and $f_3(2F)$ states, respectively. It is noteworthy that while the total widths exhibit some dependence on the screening parameter μ, the resulting width ranges (e.g., 72–235 MeV for $f_3(2F)$) along with the results obtained using experimental masses (e.g., 207 MeV) are consistent with current experimental data at $\theta = 0$, providing a self-consistent physical picture.

In addition, we provide predictions for the masses and total widths of the higher excited states at the nominal screening parameter $\mu = 78$ MeV,

$$\begin{cases} M(a_3(3F)) = 2454 \text{ MeV} \\ \Gamma(a_3(3F)) = 111 \text{ MeV} \end{cases} \begin{cases} M(a_3(4F)) = 2631 \text{ MeV} \\ \Gamma(a_3(4F)) = 78.8 \text{ MeV} \end{cases},$$

$$\begin{cases} M(f_3(3F)) = 2454 \text{ MeV} \\ \Gamma(f_3(3F)) = 96.7 \text{ MeV} \end{cases} \begin{cases} M(f_3(4F)) = 2631 \text{ MeV} \\ \Gamma(f_3(4F)) = 75.4 \text{ MeV} \end{cases},$$

$$\begin{cases} M(f_3'(1F)) = 2166 \text{ MeV} \\ \Gamma(f_3'(1F)) = 111 \text{ MeV} \end{cases} \begin{cases} M(f_3'(2F)) = 2452 \text{ MeV} \\ \Gamma(f_3'(2F)) = 145 \text{ MeV} \end{cases},$$

$$\begin{cases} M(f_3'(3F)) = 2682 \text{ MeV} \\ \Gamma(f_3'(3F)) = 127 \text{ MeV} \end{cases} \begin{cases} M(f_3'(4F)) = 2870 \text{ MeV} \\ \Gamma(f_3'(4F)) = 129 \text{ MeV} \end{cases}.$$

Furthermore, the main decay modes for these a_3, f_3, and f_3' states were analyzed. By treating the μ-variation as a systematic uncertainty, we find that the dominant decay hierarchies remain stable across the scanned parameter space, even though the absolute widths exhibit a moderate spread. The a_3 family has the following leading modes: the $1F$ state decays primarily to $\pi\rho_3(1690)$, while for the $2F$ state, the strength shifts to $\pi\rho_3(1990)$; subsequently, the $3F$ and $4F$ states both favor $\pi\rho_3(2250)$. For the f_3 family, the decay is dominated by πa_2 for the $1F$ and $2F$ states, with the preference moving to $\pi a_2(1700)$ for $3F$ and $4F$. The f_3' states—including both the ground state and higher excitations—are consistently characterized by KK_2^* as the principal final state. These stable decay patterns, combined with our mass and width predictions, provide valuable guidance for the experimental identification of the 3^{++} meson family in current and future hadronic physics experiments.

We anticipate that forthcoming experimental measurements will play a decisive role in clarifying the nature of the observed light mesons with $I^GJ^{PC} = 1^-3^{++}$ and $I^GJ^{PC} = 0^+3^{++}$, and in testing the predictions presented here.

ACKNOWLEDGMENTS

This work is supported by the National Natural Science Foundation of China under Grants No. 11965016, and No. 12247101, and by the Natural Science Foundation of Qinghai Province under Grant No. 2022-ZJ-939Q.

DATA AVAILABILITY

The data supporting the findings of this study were obtained from theoretical calculations based on the modified Godfrey-Isgur (MGI) model and the quark pair creation (QPC) model, as described in the text. These data are available from the corresponding author upon reasonable request.

[1] S. Navas *et al.* (Particle Data Group), Phys. Rev. D **110**, 030001 (2024).
[2] S. U. Chung *et al.*, Phys. Rev. D **65**, 072001 (2002).
[3] A. V. Anisovich, C. A. Baker, C. J. Batty, D. V. Bugg, V. A. Nikonov, A. V. Sarantsev, V. V. Sarantsev, and B. S. Zou, Phys. Lett. B **517**, 261 (2001).
[4] A. V. Anisovich, C. A. Baker, C. J. Batty, D. V. Bugg, V. A. Nikonov, A. V. Sarantsev, V. V. Sarantsev, and B. S. Zou, Phys. Lett. B **517**, 273 (2001).
[5] A. V. Anisovich, C. A. Baker, C. J. Batty, D. V. Bugg, C. Hodd, H. C. Lu, V. A. Nikonov, A. V. Sarantsev, V. V. Sarantsev, and B. S. Zou, Phys. Lett. B **491**, 47 (2000).
[6] D. V. Bugg, Eur. Phys. J. C **36**, 161 (2004).
[7] P. Masjuan, E. Ruiz Arriola, and W. Broniowski, Phys. Rev. D **85**, 094006 (2012).
[8] C.-Q. Pang, B. Wang, X. Liu, and T. Matsuki, Phys. Rev. D **92**, 014012 (2015).
[9] D. Ebert, R. N. Faustov, and V. O. Galkin, Phys. Rev. D **79**, 114029 (2009).
[10] S. S. Afonin, Phys. Rev. C **76**, 015202 (2007).
[11] J. J. Dudek, R. G. Edwards, B. Joó, M. J. Peardon, D. G. Richards, and C. E. Thomas, Phys. Rev. D **83**, 111502 (2011).
[12] S. Godfrey and N. Isgur, Phys. Rev. D **32**, 189 (1985).
[13] S. Godfrey, K. Moats, and E. S. Swanson, Phys. Rev. D **94**, 054025 (2016).

[14] E. Laermann, F. Langhammer, I. Schmitt, and P. M. Zerwas, Phys. Lett. B **173**, 437 (1986).
[15] K. D. Born, E. Laermann, N. Pirch, T. F. Walsh, and P. M. Zerwas, Phys. Rev. D **40**, 1653 (1989).
[16] F. Knechtli and R. Sommer (ALPHA Collaboration), Nucl. Phys. **B590**, 309 (2000).
[17] K.-T. Chao, Y.-B. Ding, and D.-H. Qin, Commun. Theor. Phys. **18**, 321 (1992).
[18] Y.-B. Ding, K.-T. Chao, and D.-H. Qin, Chin. Phys. Lett. **10**, 460 (1993).
[19] Q.-T. Song, D.-Y. Chen, X. Liu, and T. Matsuki, Phys. Rev. D **91**, 054031 (2015).
[20] J.-Z. Wang, Z.-F. Sun, X. Liu, and T. Matsuki, Eur. Phys. J. C **78**, 915 (2018).
[21] J.-Z. Wang, D.-Y. Chen, X. Liu, and T. Matsuki, Phys. Rev. D **99**, 114003 (2019).
[22] X.-Z. Weng, W.-Z. Deng, and S.-L. Zhu, Phys. Rev. D **110**, 056052 (2024).
[23] C.-Q. Pang, Phys. Rev. D **99**, 074015 (2019).
[24] C.-Q. Pang, Y.-R. Wang, H. Chen, and X.-H. Liu, arXiv: 2508.21442.
[25] L. Micu, Nucl. Phys. **B10**, 521 (1969).
[26] E. S. Ackleh, T. Barnes, and E. S. Swanson, Phys. Rev. D **54**, 6811 (1996).
[27] O. Philipsen and H. Wittig, Nucl. Phys. B, Proc. Suppl. **73**, 706 (1999).
[28] C.-Q. Pang, Y.-R. Wang, and C.-H. Wang, Phys. Rev. D **99**, 014022 (2019).
[29] Y.-R. Wang, T.-Y. Li, Z.-Y. Fang, H. Chen, and C.-Q. Pang, Phys. Rev. D **106**, 114024 (2022).
[30] L.-M. Wang, S.-Q. Luo, and X. Liu, Phys. Rev. D **105**, 034011 (2022).
[31] X.-C. Feng, Z.-Y. Li, D.-M. Li, Q.-T. Song, E. Wang, and W.-C. Yan, Phys. Rev. D **106**, 076012 (2022).
[32] L.-M. Wang, W.-X. Tian, T.-Y. Li, C.-X. Liu, and X. Liu, Phys. Rev. D **110**, 114049 (2024).
[33] Y.-R. Wang, X.-H. Liu, C.-Q. Pang, and H. Chen, Phys. Rev. D **111**, 054005 (2025).
[34] C.-Q. Pang, H. Chen, and Y.-H. Zhang, Phys. Rev. D **112**, 036017 (2025).
[35] A. Le Yaouanc, L. Oliver, O. Pène, and J. C. Raynal, Phys. Rev. D **8**, 2223 (1973).
[36] A. Le Yaouanc, L. Oliver, O. Pène, and J. C. Raynal, Phys. Rev. D **9**, 1415 (1974).
[37] A. Le Yaouanc, L. Oliver, O. Pène, and J. C. Raynal, Phys. Rev. D **11**, 1272 (1975).
[38] A. Le Yaouanc, L. Oliver, O. Pène, and J. C. Raynal, Phys. Lett. **72B**, 57 (1977).
[39] A. Le Yaouanc, L. Oliver, O. Pène, and J. C. Raynal, Phys. Lett. **71B**, 397 (1977).
[40] E. van Beveren, G. Rupp, T. A. Rijken, and C. Dullemond, Phys. Rev. D **27**, 1527 (1983).
[41] A. I. Titov, T. I. Gulamov, and B. Kämpfer, Phys. Rev. D **53**, 3770 (1996).
[42] H. G. Blundell, arXiv:hep-ph/9608473.
[43] R. Bonnaz, B. Silvestre-Brac, and C. Gignoux, Eur. Phys. J. A **13**, 363 (2002).
[44] H.-Q. Zhou, R.-G. Ping, and B.-S. Zou, Phys. Lett. B **611**, 123 (2005).
[45] J. Lu, X.-L. Chen, W.-Z. Deng, and S.-L. Zhu, Phys. Rev. D **73**, 054012 (2006).
[46] B. Zhang, X. Liu, W.-Z. Deng, and S.-L. Zhu, Eur. Phys. J. C **50**, 617 (2007).
[47] Z.-G. Luo, X.-L. Chen, and X. Liu, Phys. Rev. D **79**, 074020 (2009).
[48] Z.-F. Sun and X. Liu, Phys. Rev. D **80**, 074037 (2009).
[49] X. Liu, Z.-G. Luo, and Z.-F. Sun, Phys. Rev. Lett. **104**, 122001 (2010).
[50] Z.-F. Sun, J.-S. Yu, X. Liu, and T. Matsuki, Phys. Rev. D **82**, 111501 (2010).
[51] T. A. Rijken, M. M. Nagels, and Y. Yamamoto, Nucl. Phys. **A835**, 160 (2010).
[52] Z.-C. Ye, X. Wang, X. Liu, and Q. Zhao, Phys. Rev. D **86**, 054025 (2012).
[53] X. Wang, Z.-F. Sun, D.-Y. Chen, X. Liu, and T. Matsuki, Phys. Rev. D **85**, 074024 (2012).
[54] L.-P. He, X. Wang, and X. Liu, Phys. Rev. D **88**, 034008 (2013).
[55] Y. Sun, X. Liu, and T. Matsuki, Phys. Rev. D **88**, 094020 (2013).
[56] Y.-R. Wang, Y. Ma, and C.-Q. Pang, Int. J. Mod. Phys. A **38**, 2350118 (2023).
[57] T.-Y. Li, Y.-R. Wang, and C.-Q. Pang, Phys. Rev. D **107**, 074008 (2023).
[58] T.-Y. Li, L. Tang, Z.-Y. Fang, C.-H. Wang, and C.-Q. Pang, Phys. Rev. D **108**, 034019 (2023).
[59] L.-M. Wang, Q.-S. Zhou, C.-Q. Pang, and X. Liu, Phys. Rev. D **102**, 114034 (2020).
[60] C.-Q. Pang, J.-Z. Wang, X. Liu, and T. Matsuki, Eur. Phys. J. C **77**, 861 (2017).
[61] J.-C. Feng, X.-W. Kang, Q.-F. Lü, and F.-S. Zhang, Phys. Rev. D **104**, 054027 (2021).
[62] M. Jacob and G. C. Wick, Ann. Phys. (N.Y.) **7**, 404 (1959).
[63] H.-Y. Cheng, Proc. Sci., Hadron2013 (**2013**) 090 [arXiv: 1311.2370].
[64] I. Asghar, F. Akram, B. Masud, and M. A. Sultan, Phys. Rev. D **100**, 096002 (2019).
[65] S. Godfrey, AIP Conf. Proc. **132**, 262 (1985).
[66] G. S. Bali, H. Neff, T. Duessel, T. Lippert, and K. Schilling (SESAM Collaboration), Phys. Rev. D **71**, 114513 (2005).
[67] J. Vijande, F. Fernández, and A. Valcarce, J. Phys. G **31**, 481 (2005).
[68] X.-Y. Chen, Y. Tan, Y. Chen, X.-J. Liu, and J.-L. Ping, Mod. Phys. Lett. A **41**, 2650044 (2026).
[69] R. Machleidt, K. Holinde, and C. Elster, Phys. Rep. **149**, 1 (1987).
[70] L. Y. Glozman and D. O. Riska, Phys. Rep. **268**, 263 (1996).
[71] A. Valcarce, H. Garcilazo, F. Fernández, and P. González, Rep. Prog. Phys. **68**, 965 (2005).
[72] J. Vijande, A. Valcarce, and K. Tsushima, Phys. Rev. D **74**, 054018 (2006).
[73] U. Taboada-Nieto, P. G. Ortega, D. R. Entem, F. Fernández, and J. Segovia, Eur. Phys. J. A **59**, 40 (2023).
[74] D. R. Entem, F. Fernández, P. G. Ortega, and J. Segovia, arXiv:2504.07897.
[75] Y. Tan, X.-J. Liu, X.-Y. Chen, H.-X. Huang, and J.-L. Ping, Phys. Rev. D **108**, 014017 (2023).